

# Stochastic statistical theory of nucleation and evolution of nano-sized precipitates in alloys with application to precipitation of copper in iron

K. Yu. Khromov<sup>a</sup>, F. Soisson<sup>b</sup>, A. Yu. Stroev<sup>a</sup> and V. G. Vaks<sup>a</sup>

<sup>a</sup>*Russian Research Center "Kurchatov Institute", 123182 Moscow, Russia*

<sup>b</sup>*Service de Recherches de Métallurgie Physique, DMN-SRMP, CEA Saclay, 91191 Gif-sur-Yvette, France*

(Dated: November 5, 2018)

The consistent and computationally efficient stochastic statistical approach (SSA) is suggested to study kinetics of nucleation and evolution of nano-sized precipitates in alloys. An important parameter of the theory is the size of locally equilibrated regions at the nucleation stage which is estimated using the “maximum thermodynamic gain” principle suggested. For several realistic models of iron-copper alloys studied, the results of the SSA-based simulations of precipitation kinetics agree well with the kinetic Monte Carlo simulation results for all main characteristics of microstructure. The approach developed is also used to study kinetics of nucleation and changes in microstructural evolution under variations of temperature or concentration.

PACS numbers: 05.70.Fh; 05.10.Gg

## I. INTRODUCTION

Studies of microstructural evolution in phase-separating alloys attract interest from both fundamental and applied points of view. From the fundamental side, elucidation of microscopic mechanisms for the formation and evolution of embryos of new phases arising under the first-order phase transitions is one of the principal problems in statistical physics being not well understood as yet [1–4]. From the applied side, understanding factors that determine different characteristics of microstructure formed under precipitation is important to control these characteristics, particularly for alloys with nano-sized precipitates which attract recently much attention in connection with industrial applications [5–8].

Presently, theoretical studies of the precipitation kinetics employ usually either the phase-field method (PFM) [9–14] or Monte Carlo modeling [4, 15–18]. However, employing the phase-field methods to describe nucleation and evolution of nano-sized precipitates can be misleading for at least three reasons. First, the “continuous” approximation used in the PFM disregards the discrete lattice effects which should be important at first stages of nucleation when typical precipitate sizes are few lattice constants. Second, at the concentration and temperature values typical for applications, the mean-field-type CALPHAD expressions for thermodynamic potentials usually employed in the PFM studies [9–13] will be shown to strongly distort the position of spinodals, thus using these expressions can drastically distort the type of microstructural evolution. Third, treatment of fluctuative terms (being crucial for the nucleation stage) in the “stochastic PFM” versions used in applications until now [9, 10] seems to be arbitrary and inconsistent [19, 20], while the adequate description of these terms determines all main characteristics of microstructure.

Therefore, the only reliable source of theoretical information about nucleation and evolution of nano-sized precipitates now is Monte Carlo modeling, in particular,

the kinetic Monte Carlo approach (KMCA) developed in Refs. [4, 15–18]. However, present versions of the KMCA are time-consuming, which may partly explain a relatively few number of applications of this method to concrete systems [17, 18]. Moreover, the lattice misfit and elastic strain effects important for many phase-separating alloys can not be easily taken into account in the KMCA, while it makes no problem for statistical approaches [21]. Finally, in the KMCA it is often difficult to follow the dependence of various characteristics of evolution on thermodynamic and microscopic parameters of an alloy, such as the composition, temperature, different interaction constants, etc, while it is usually much simpler for statistical methods based on some analytical equations. Therefore, the development of a consistent statistical theory which takes into account all achievements of the KMCA seems to be very important for a more deep understanding of the phase separation kinetics.

Recently Stroev et al. [20] (SPV) presented an attempt to develop such a theory using the stochastic statistical approach (SSA) described below in Sec. III B. To illustrate the main ideas of this approach, SPV used only simplest methods and models, such as the mean-field approximation (MFA), continuous approximations, the direct-atomic-exchange rather than the vacancy exchange kinetic model, oversimplified interaction models, etc, while no attempts of quantitative treatments for realistic alloy models have been made.

The main aim of the present work is to raise the accuracy and the predictive power of the SSA in describing the precipitation kinetics for realistic alloy models up to the level comparable to that of the KMCA. To this end, we perform detailed studies of nucleation and evolution of nano-sized precipitates in Fe-Cu alloys using both the KMCA [16, 17] and the SSA. This requires many refinements of simple models used by SPV. We have to consider the realistic vacancy-mediated exchange kinetics rather than the simplified direct-atomic-exchange model; to use the quantitative, cluster statistical methods rather than

the simple MFA; to allow for strong concentration and temperature dependences of generalized mobilities in the resulting kinetic equations, etc. All these refinements are made in the present work. We also introduce the “maximum thermodynamic gain” principle to determine the key kinetic parameter of the SSA, the characteristic length of local equilibrium in the course of the nucleation process.

In Sec. II we discuss the methodological problems mentioned above: generalizations of our statistical approach to the vacancy-mediated kinetics case; employing cluster methods for both thermodynamic and kinetic statistical calculations; elaboration of effective methods for calculations of effective mobilities which enter resulting kinetic equations, etc. Here we also generalize the earlier-suggested “equivalence theorem” [22] which enables us to reduce the vacancy-mediated kinetics to that for some equivalent direct-exchange models. In Sec. III we remind basic ideas of the classical theory of nucleation and present the main equations of the SSA. In Sec. IV we discuss the models and the methods of simulations used and we describe the “maximum thermodynamic gain” principle suggested to estimate the local equilibrium length mentioned above. In Sec. V we discuss the features of microstructural evolution observed in the KMCA and SSA simulations for various alloy states considered. Here we also use the SSA to study kinetics of nucleation and influence of variations of temperature or concentration on evolution of microstructure. Our main conclusions are summarized in Sec. VI.

## II. QUASI-EQUILIBRIUM KINETIC EQUATION FOR VACANCY-MEDIATED KINETICS IN SUBSTITUTIONAL ALLOY

### A. General equations for mean occupations of lattice sites

In this section we derive kinetic equations for mean occupations of lattice sites disregarding fluctuations of atomic fluxes which lead to local violations of the second law of thermodynamics. These “quasi-equilibrium kinetic equations” (QKE) differ from the stochastic kinetic equations discussed below (which take into account such fluctuations) and generalize those used by SPV [20] for simplified direct-atomic-exchange models to more realistic, vacancy-mediated-exchange (VME) models. Here we also generalize a similar treatment of the VME kinetics made by Belashchenko and Vaks [22] (BV) to more realistic VME models used in Refs. [16, 17] and below.

We consider a substitutional alloy with  $(m + 1)$  components  $p'$  which includes atoms of  $m$  different species  $p = p_1, p_2, \dots, p_m$  and vacancies  $v$ :  $p' = \{p, v\}$ . The distributions of atoms on the lattice sites  $i$  are described by the different occupation number sets  $\{n_i^{p'}\}$  where the operator  $n_i^{p'}$  is 1 when the site  $i$  is occupied by a  $p'$ -species component and 0 otherwise. For each  $i$  these operators

obey the identity  $\sum_{p'} n_i^{p'} = 1$ , so only  $m$  of them are independent. It is convenient to mark the independent operators with greek letters  $\rho$  or  $\sigma$ :  $(n_i^{p'})_{\text{indep}} = n_i^\rho$ , while the rest operator denoted as  $n_i^h$  is expressed via  $n_i^\rho$ :

$$n_i^h = 1 - \sum_{\rho} n_i^\rho. \quad (1)$$

For dilute alloys, it is convenient to put “ $h$ ” in (1) to be the host component, e.g.,  $h = \text{Fe}$  for FeCuv alloys.

In terms of all operators  $n_i^{p'}$  the configurational Hamiltonian  $H'$  (for simplicity supposed to be pairwise) can be written as

$$H' = \frac{1}{2} \sum_{p'q', ij} V_{ij}^{p'q'} n_i^{p'} n_j^{q'}. \quad (2)$$

After elimination of operators  $n_i^h$  according to (1), the Hamiltonian (2) takes the form

$$H = E_0 + \sum_{\rho i} \varphi_{\rho} n_i^{\rho} + H_{\text{int}} \\ H_{\text{int}} = \sum_{\rho\sigma, i>j} v_{ij}^{\rho\sigma} n_i^{\rho} n_j^{\sigma} \quad (3)$$

which includes only independent  $n_i^\rho$ , while constants  $E_0$ ,  $\varphi_{\rho}$ , and “configurational interactions”  $v_{ij}^{\rho\sigma}$  are linearly expressed via the interactions  $V_{ij}^{p'q'}$  in (2), in particular:

$$v_{ij}^{\rho\sigma} = (V^{\rho\sigma} - V^{\rho h} - V^{h\sigma} + V^{hh})_{ij}. \quad (4)$$

The fundamental master equation for the probability  $P$  of finding the occupation number set  $\{n_i^\rho\} = \xi$  is [21]:

$$dP(\xi)/dt = \sum_{\eta} [W(\xi, \eta)P(\eta) - W(\eta, \xi)P(\xi)] \equiv \hat{S}P \quad (5)$$

where  $W(\xi, \eta)$  is the  $\eta \rightarrow \xi$  transition probability per unit time. Adopting for probabilities  $W$  the conventional “transition state” model [4, 15–17], we can express the transfer matrix  $\hat{S}$  in (5) in terms of the probability of an elementary inter-site exchange (“jump”)  $pi \rightleftharpoons vj$  between neighboring sites  $i$  and  $j$ :

$$W_{ij}^{pv} = n_i^p n_j^v \omega_{pv} \exp[-\beta(\hat{E}_{pi,vj}^{SP} - \hat{E}_{pi,vj}^{in})] \quad (6)$$

where  $\omega_{pv}$  is the attempt frequency,  $\beta = 1/T$  is the reciprocal temperature,  $\hat{E}_{pi,vj}^{SP}$  is the saddle point energy, and  $\hat{E}_{pi,vj}^{in}$  is the initial (before the jump) configurational energy of a jumping atom  $p$  and a vacancy. The saddle point energy  $\hat{E}_{pi,vj}^{SP}$ , generally, depends on the atomic configuration near the bond  $ij$  (which is neglected in simplified kinetic models [4, 15, 22]). We will describe this dependence by the model used in Refs. [16] and [17] supposing the saddle-point energy to depend only

on occupations of lattice sites  $l$  nearest to the center of bond  $ij$  (these sites will be denoted  $l_{nn}^{ij}$ ):

$$\hat{E}_{pi,vj}^{SP} = \sum_{q, l=l_{nn}^{ij}} \varepsilon_q^p n_l^q = E_h^p - \hat{\Delta}_{ij}^p. \quad (7)$$

Here  $E_h^p$  is the saddle point energy for the pure host metal, while the operator  $\hat{\Delta}_{ij}^p$  describes changes in this energy due to a possible presence of minority atoms near the bond:

$$E_h^p = z_{nn}^b \varepsilon_h^p; \quad \hat{\Delta}_{ij}^p = \sum_{\rho, l=l_{nn}^{ij}} \Delta_{\rho}^p n_l^{\rho} \quad (8)$$

where  $z_{nn}^b$  is the total number of nearest lattice sites  $l$  for each bond (being  $z_{nn}^b = 6$  for the BCC lattice), and  $\Delta_{\rho}^p = (\varepsilon_h^p - \varepsilon_{\rho}^p)$ .

As discussed in detail in [21], for the usual conditions of phase transitions corresponding to absence of external fluxes of particles or energy (that is, when the alloy is a “closed” but not an “open” statistical system), the distribution function  $P(\xi) = P\{n_i^{\rho}\}$  in (5) can be written as

$$P\{n_i^{\rho}\} = \exp \left[ \beta(\Omega + \sum_{\rho i} \lambda_i^{\rho} n_i^{\rho} - H_{int}) \right]. \quad (9)$$

Here parameters  $\lambda_i^{\rho}$  (being, generally, both time- and space-dependent) can be called “site chemical potentials” for  $\rho$ -species atoms;  $H_{int}$  is the same as in (3); and the generalized grand canonical potential  $\Omega$  is determined by normalization. The analogous equation (10) of BV [22] (who treated both closed and open systems) differs from (9) with replacing the interaction hamiltonian by a more general “quasi-interaction” operator  $Q$ . For the closed systems discussed in this work,  $Q = H_{int}$ , and this relation greatly simplifies kinetic equations discussed below with respect to those of BV.

Multiplying Eq. (5) by operators  $n_i^{\rho}$  and summing over all configurational states, i.e. over all number sets  $\{n_i^{\rho}\}$ , we obtain the set of equations for mean occupations of sites (“local concentrations”)  $c_i^{\rho} = \langle n_i^{\rho} \rangle$ :

$$dc_i^{\rho}/dt = \langle n_i^{\rho} \hat{S} \rangle \quad (10)$$

where  $\langle \dots \rangle = \text{Tr}\{(\dots)P\}$  means averaging over the distribution  $P$ , for example:

$$c_i^{\rho} = \langle n_i^{\rho} \rangle = \sum_{\{n_j^{\sigma}\}} c_i^{\rho} P\{n_j^{\sigma}\}. \quad (11)$$

After a number of manipulations described by BV, Eqs. (10) can be transformed into the QKE for mean occupations  $c_i^{\rho}$ . These equations are similar to Eqs. (19) and (42) of BV but include generalizations and simplifi-

cations mentioned above:

$$\begin{aligned} dc_i^{\alpha}/dt &= \sum_{j_{nn}(i)} \gamma_{\alpha v} b_{ij}^{\alpha} (\xi_i^v \eta_j^{\alpha} - \xi_j^v \eta_i^{\alpha}) \quad (12) \\ dc_i^v/dt &= \sum_{j_{nn}(i)} \left[ \xi_j^v \left( \gamma_{hv} b_{ij}^h + \sum_{\beta} \gamma_{\beta v} b_{ij}^{\beta} \eta_i^{\beta} \right) \right. \\ &\quad \left. - \{i \rightarrow j\} \right]. \quad (13) \end{aligned}$$

Here and below, greek indices  $\alpha, \beta \dots$  correspond to the minority atoms; symbol “v” is used for vacancies; index  $nn$  means “nearest neighbors”, and symbol “ $j_{nn}(i)$ ” means summation over sites  $j$  being nearest neighbors of site  $i$ . Term  $\gamma_{pv}$  in (13) (where  $p$  is  $\alpha$  or  $h$ , i. e. a minority or host atom) is the effective exchange rate  $p \rightleftharpoons v$  for a pure host metal. This term can be written in the form similar to Eq. (6):

$$\gamma_{pv} = \omega_{pv} \exp(-\beta E_{ac}^{pv}) \quad (14)$$

where  $\omega_{pv}$  is the same as in (6), while  $E_{ac}^{pv}$  is the effective activation energy which is expressed via the saddle point energies  $E_h^p$  in (8) and interactions  $V_{ij}^{p'q'}$  in (2) as follows:

$$E_{ac}^{pv} = E_h^p - \sum_j (V_{ij}^{ph} + V_{ij}^{vh}) + V_{nn}^{hh}. \quad (15)$$

Note that for minority atoms  $p=\alpha$ , expressions (15) differ from analogous activation energies  $E_{ac,MC}^{pv}$  used in the KMCA and given by Eq. (2.5) in Ref. [16]:

$$E_{ac}^{\alpha v} = E_{ac,MC}^{\alpha v} + v_{nn}^{\alpha v}; \quad E_{ac}^{hv} = E_{ac,MC}^{hv}. \quad (16)$$

The difference arises because in the statistically averaged Eqs. (12) and (13), the probability (6) is averaged over distribution (9), and for the inter-site exchange  $\alpha i \rightleftharpoons v j$ , it leads to the additional Gibbs factor  $\exp(-\beta v_{ij}^{\alpha v})$  in the averaged probability.

Quantities  $b_{ij}^p$  in (13) (for brevity to be called “correlators”) are certain averages of site occupations which describe influence of minority atoms in vicinity of the bond  $ij$  on the  $pi \rightleftharpoons vj$  jump probability:

$$b_{ij}^p = \langle n_i^h n_j^h \exp \left[ \sum_{\alpha l} \beta (u_{il}^{\alpha} + u_{jl}^{\alpha}) n_l^{\alpha} + \sum_{\alpha, l=l_{nn}^{ij}} \beta \Delta_{\alpha}^p n_l^{\alpha} \right] \rangle \quad (17)$$

where  $\Delta_{\alpha}^p$  is the same as in (8), while quantities  $u_{il}^{\alpha}$  (to be called “kinetic interactions” as they affect only effective jump probabilities but not thermodynamic properties) are related to the interactions  $V_{ij}^{p'q'}$  in (2) as follows:

$$u_{il}^{\alpha} = V_{il}^{\alpha h} - V_{il}^{hh}. \quad (18)$$

Finally, quantities  $\xi_i^v$  and  $\eta_i^{\alpha}$  in (13) and (12) can be called “site thermodynamic activities” for vacancies and  $\alpha$ -species atoms, respectively, as they are related to site chemical potentials  $\lambda_i^{\rho}$  in (9) as:

$$\xi_i^v = \exp(\beta \lambda_i^v); \quad \eta_i^{\alpha} = \exp(\beta \lambda_i^{\alpha}), \quad (19)$$

that is, analogously to the relations between conventional thermodynamic activities and chemical potentials.

## B. Calculations of site chemical potentials $\lambda_i^p$ and correlators $b_{ij}^p$

To solve QKE (13), we need explicit expressions for site chemical potentials  $\lambda_i^p = \lambda_i^p(c_j)$  determined by Eqs. (11), and for correlators  $b_{ij}^p = b_{ij}^p(c_k)$  determined by Eqs. (17). To find these expressions, we should use some approximate method of statistical physics, such as the MFA or cluster methods [21]. As discussed in detail in [24, 25] and below, at realistic values of interactions  $v_{ij}^{\alpha\beta}$  that significantly exceed temperature  $T$  (which is typical, in particular, for the iron-copper alloys under consideration), employing the MFA leads to great errors in calculations of thermodynamic potentials which exclude any realistic description. At the same time, the pair cluster approximation (PCA) usually combines simplicity of calculations with a rather high accuracy, particularly at low  $c$  and  $T$  under consideration, see, e. g. [24–26]. Thus, for site the chemical potentials  $\lambda_i^p$  we use their PCA-expressions which for a binary alloy ABv with minority atoms A, host atoms B, and a realistically small concentration of vacancies:  $c_i^v \ll 1$ , are given by Eqs. (39) of BV:

$$\lambda_i = T \left[ \ln(c_i/c_i^h) + \sum_{j \neq i} \ln(1 - g_{ij}c_j) \right] \quad (20)$$

$$\lambda_i^v = T \left[ \ln(c_i^v/c_i^h) - \sum_{j \neq i} \ln(1 + g_{ij}^v c_j) \right]. \quad (21)$$

Here  $\lambda_i = \lambda_i^A$ ,  $c_i = c_i^A$ ,  $c_i^h = (1 - c_i - c_i^v) \simeq (1 - c_i)$ , while the function  $g_{ij}$  or  $g_{ij}^v$  is expressed via the Mayer function  $f_{ij} = [\exp(-\beta v_{ij}) - 1]$  or  $f_{ij}^v = [\exp(-\beta v_{ij}^v) - 1]$  for the potential  $v_{ij} \equiv v_{ij}^{AA}$  or  $v_{ij}^v \equiv v_{ij}^{AA}$  defined in (4),

$$\begin{aligned} v_{ij} &= V_{ij}^{AA} - 2V_{ij}^{AB} + V_{ij}^{BB} \\ v_{ij}^v &= V_{ij}^{vA} - V_{ij}^{vB} - V_{ij}^{AB} + V_{ij}^{BB}, \end{aligned} \quad (22)$$

as follows:

$$\begin{aligned} g_{ij} &= 2f_{ij}/[R_{ij} + 1 + f_{ij}(c_i + c_j)] \\ g_{ij}^v &= 2f_{ij}^v/[R_{ij} + 1 + f_{ij}(c_i - c_j)] \\ R_{ij} &= \{[1 + (c_i + c_j)f_{ij}]^2 - 4c_i c_j f_{ij}(f_{ij} + 1)\}^{1/2}. \end{aligned} \quad (23)$$

Let us also present the PCA expression for the free energy  $F$  of a binary alloy [21] which is used below in Sec. IV B for discussions of thermodynamics of precipitation:

$$F = \sum_i T \ln c_i^h - T \frac{1}{2} \sum_{ij} \ln(1 - g_{ij}c_i c_j) + \sum_i \lambda_i c_i \quad (24)$$

where  $g_{ij}$  is the same as in (23). If temperature  $T$ , much exceeds interactions  $v_{ij}$ :  $T \gg v_{ij}$ , the PCA expressions (20) and (24) transform into the MFA ones [21]. However, as mentioned, in situations of practical interest we usually have an opposite inequality:  $T \ll v_{ij}$ , and employing the MFA is misleading.

Let us now discuss calculations of correlators  $b_{ij}^p$  in (17). For simplicity, we first consider the case of configuration-independent saddle-point energies when differences  $\Delta_\alpha^p$  in Eqs. (8) and (17) vanish and correlators  $b_{ij}^p = b_{ij}$  do not depend on the kind of a jumping atom  $p$ . Using identities

$$\begin{aligned} (n_i^\alpha)^2 &= n_i^\alpha, \quad n_i^\alpha n_i^\beta = n_i^\alpha \delta_{\alpha\beta}, \quad n_i^\alpha n_i^h = 0, \\ \exp(xn_i^\alpha) &= 1 + n_i^\alpha f(x), \quad f(x) = (e^x - 1), \end{aligned} \quad (25)$$

we can rewrite Eq. (17) for this case as follows:

$$\begin{aligned} b_{ij} &= \left\langle n_i^h n_j^h \prod_{l=1}^{k_t} (1 + \sum_\alpha f_l^\alpha n_l^\alpha) \right\rangle = \\ &= \sum_{k=0}^{k_t} \sum_{l_1 \neq \dots \neq l_k} \sum_{\alpha_1 \dots \alpha_k} \left\langle n_i^h n_j^h n_{l_1}^{\alpha_1} \dots n_{l_k}^{\alpha_k} \right\rangle f_{l_1}^{\alpha_1} \dots f_{l_k}^{\alpha_k} \end{aligned} \quad (26)$$

where quantity  $f_l^\alpha$  is defined as

$$f_l^\alpha = f(\beta u_{il}^\alpha + \beta u_{jl}^\alpha) \quad (27)$$

with  $f(x)$  from (25), while  $k_t$  in (26) is the total number of sites with nonzero values of potentials ( $u_{il}^\alpha + u_{jl}^\alpha$ ). For example, for the nearest-neighbor or second-neighbor interaction models in the BCC lattice, we have:  $k_t = 14$ , or:  $k_t = 20$ .

To find averages in (26) over distribution (9), we should again employ some approximate method of calculations, such as the MFA, PCA or higher-order cluster approximations [21, 26]. However, for the most of systems of practical interest, in particular, for the iron-copper alloys discussed below, we can apparently use in (26) the simple MFA replacing each operator  $n_l^\alpha$  by its average value  $c_l^\alpha = \langle n_l^\alpha \rangle$ . It seems to be justified as the functions  $f_l^\alpha$  in Eqs. (26) and (27) for such systems are typically rather large (for example,  $f(\beta u_1) \gtrsim 5$  for the systems described by Table III below). Thus the main contributions to sum (26) come from averages of products of many different operators  $n_l^\alpha$  which correspond to well-separated and weakly correlated sites  $l$ . In particular, for the BCC lattice, these products (even for the nearest-neighbor interaction model) include terms with the neighbors from first to tenth, most often third and fourth. Correlations of occupations for the so distant lattice sites should be typically small, thus using the MFA that neglects such correlations should be adequate.

In the MFA, Eq. (26) takes the form

$$b_{ij} = c_i^h c_j^h \sum_{k=0}^{k_t} \sum_{l_1 \neq \dots \neq l_m \neq i, j} \sum_{\alpha_1 \dots \alpha_k} c_{l_1}^{\alpha_1} \dots c_{l_k}^{\alpha_k} f_{l_1}^{\alpha_1} \dots f_{l_k}^{\alpha_k}. \quad (28)$$

To further simplify this expression, we can take into account that the space variations of local concentration  $c_l^\alpha$  arising in the course of alloy decomposition are typically rather smooth, particularly at the nucleation stage (for which an adequate description of kinetic coefficients that

include correlators  $b_{ij}$  is most important), see, e. g. Figs. 20-22 below. Thus, the  $c_l^\alpha$  values for sites  $l$  adjacent to bond  $ij$  that enter Eq. (28) are usually close to both the  $c_i^\alpha$  and  $c_j^\alpha$ , as well as to their average

$$\bar{c}_{ij}^\alpha = (c_i^\alpha + c_j^\alpha)/2. \quad (29)$$

Therefore, to avoid unnecessary complications of computations, we can approximate each  $c_l^\alpha$  in Eq. (28) by the average (29). It enables us to write the correlator  $b_{ij}$  (28) in the simple analytic form:

$$b_{ij} = c_i^h c_j^h \prod_{l \neq i, j}^{k_t} (1 + \sum_{\alpha} \bar{c}_{ij}^\alpha f_l^\alpha). \quad (30)$$

For example, for a binary alloy ABv in the BCC lattice described by the second-neighbor interaction model with two kinetic interaction constants,  $u_1$  and  $u_2$ , we obtain:

$$b_{ij} = c_i^h c_j^h [1 + \bar{c}_{ij} f(\beta u_1 + \beta u_2)]^6 \times [1 + \bar{c}_{ij} f(\beta u_1)]^8 [1 + \bar{c}_{ij} f(\beta u_2)]^6 \quad (31)$$

where index  $\alpha = A$  in  $c_{ij}^\alpha$  and  $u_n^\alpha$  is omitted for brevity.

When differences  $\Delta_\alpha^p$  in Eqs. (8) and (17) are nonzero, the correlator  $b_{ij}^p$  in Eq. (17) can be calculated by the same way as  $b_{ij}$  in Eqs. (26)-(31). The difference arises only for sites  $l = l_{nn}^{ij}$  adjacent to bond  $ij$  for which factors  $f_l^\alpha$  defined by Eq. (27) are now replaced by analogous factors  $f_{\Delta}^{\alpha p}$  defined as:

$$f_{\Delta}^{\alpha p} = f(\beta u_{il}^\alpha + \beta u_{jl}^\alpha + \beta \Delta_\alpha^p). \quad (32)$$

In particular, for the BCC binary alloy ABv with the second-neighbor interaction, we obtain instead of (31):

$$b_{ij}^p = c_i^h c_j^h [1 + \bar{c}_{ij} f_{\Delta}^{\alpha p}]^6 \times [1 + \bar{c}_{ij} f(\beta u_1)]^8 [1 + \bar{c}_{ij} f(\beta u_2)]^6 \quad (33)$$

where  $f_{\Delta}^{\alpha p} = f[\beta(u_1 + u_2 + \Delta^p)]$ , and  $\Delta^p = (\varepsilon_h^p - \varepsilon_A^p)$ .

### C. Equivalence of precipitation kinetics for the vacancy-mediated exchange models to that for certain direct exchange models

In this section we show that the VME kinetics described by Eqs. (12) and (13) can usually be described in terms of certain equivalent direct-atomic-exchange (DAE) models. It will generalize the analogous “equivalence theorem” derived by BV.

First we note that the vacancy activity  $\xi_i^v = \exp(\beta \lambda_i^v)$  in Eqs. (12) and (13) is proportional to the vacancy concentration  $c_i^v$ . It is illustrated by Eqs. (21) and is actually a general relation of thermodynamics of dilute solutions. Thus time derivatives of mean occupations are proportional to the local vacancy concentration  $c_i^v$  or  $c_j^v$ , which is natural for the vacancy-mediated kinetics. As

$c_i^v$  in real alloys is very small, this implies that the relaxation times of atomic distribution  $\{c_i^\alpha\}$  are by a factor  $1/c_i^v$  greater than the time of relaxation of vacancies at the given  $\{c_i^\alpha\}$  to their “quasi-equilibrium” distribution  $c_i^v \{c_i^\alpha\}$  for which the right-hand side of Eq. (13) vanishes. Therefore, discarding small corrections of the relative order  $c_i^v \ll 1$ , we can rewrite Eq.(13) as follows:

$$0 = \sum_{j_{nn}(i)} \left[ \xi_j^v \left( \gamma_{hv} b_{ij}^h + \sum_{\alpha} \gamma_{\alpha v} b_{ij}^\alpha \eta_i^\alpha \right) - \{i \rightarrow j\} \right]. \quad (34)$$

which can be called “the adiabaticity equation” for the vacancy activity  $\xi_i^v$ . Solving this equation we can, in principle, express  $\xi_i^v$  via  $c_j^\alpha$ . Then substitution of these  $\xi_i^v(c_j^\alpha)$  into Eq. (12) yields the QKE for some equivalent DAE model.

To illustrate this approach, we first consider the VME models with configuration-independent saddle-point energies. For such models, parameters  $\Delta_\rho^p$  in (8) are zero, correlators  $b_{ij}^p = b_{ij}$  do not depend on the kind  $p$  of jumping atom, and the adiabaticity equation (34) takes the simple form:

$$\sum_{j_{nn}(i)} b_{ij} \xi_i^v \xi_j^v \left[ \left( \gamma_{hv} + \sum_{\alpha} \gamma_{\alpha v} \eta_i^\alpha \right) / \xi_i^v - \{i \rightarrow j\} \right] = 0 \quad (35)$$

If we denote the first term in square brackets (35) as  $1/\nu_i$ , then the difference in these brackets takes the form  $\nu_i^{-1} - \nu_j^{-1}$ . Thus the solution of Eqs. (35) is provided by  $\nu_i$  being a constant independent of the site number  $i$  (though possibly depending on time, as well as on temperature and other external parameters):

$$\nu_i = \xi_i^v / \left( \gamma_{hv} + \sum_{\alpha} \gamma_{\alpha v} \eta_i^\alpha \right) = \nu(t). \quad (36)$$

Relation (36) determines the above-mentioned “quasi-equilibrium” vacancy distribution  $c_i^v \{c_i^\alpha\}$  which adiabatically fast follows the atomic distribution  $\{c_i^\alpha\}$ . Substituting it into Eq. (12) we obtain the explicit kinetic equation for atomic distributions  $\{c_i^\alpha\}$  for which influence of vacancies is characterized by a single parameter  $\nu(t)$  being a “spatially self-averaged” quantity:

$$dc_i^\alpha / dt = \sum_{j_{nn}(i)} b_{ij} \nu(t) \left[ \gamma_{\alpha v} \gamma_{hv} \left( \eta_j^\alpha - \eta_i^\alpha \right) + \sum_{\beta} \gamma_{\alpha v} \gamma_{\beta v} \left( \eta_j^\alpha \eta_i^\beta - \eta_i^\alpha \eta_j^\beta \right) \right]. \quad (37)$$

The last term of this equation (missed in the analogous Eq. (46) of BV) is present only for many-component alloys with two or more species of minority atoms. Eqs. (37) can also be rewritten in the form used for DAE models [21]:

$$dc_i^\alpha / dt = \sum_{j_{nn}(i)} M_{ij}^{\alpha h} 2 \sinh[\beta(\lambda_j^\alpha - \lambda_i^\alpha)/2] + \sum_{j_{nn}(i), \beta} M_{ij}^{\alpha \beta} 2 \sinh[\beta(\lambda_j^\alpha + \lambda_i^\beta - \lambda_i^\alpha - \lambda_j^\beta)/2] \quad (38)$$

where generalized mobilities  $M_{ij}^{\text{Pq}}$  which describe inter-site exchanges  $\alpha \rightleftharpoons \text{p}$  and  $\alpha \rightleftharpoons \beta$  are given by the following expressions:

$$M_{ij}^{\alpha h} = \gamma_{\alpha v} \gamma_{h v} \nu(t) b_{ij} \exp[\beta(\lambda_i^\alpha + \lambda_j^\alpha)/2] \quad (39)$$

$$M_{ij}^{\alpha \beta} = \gamma_{\alpha v} \gamma_{\beta v} \nu(t) b_{ij} \exp[\beta(\lambda_i^\alpha + \lambda_j^\alpha + \lambda_i^\beta + \lambda_j^\beta)/2]. \quad (40)$$

Comparing these expressions to Eq. (32) of BV for mobilities  $M_{ij}^{\text{Pq}}$  in an alloy with the nearest-neighbor direct-exchange rates  $\gamma_{ij}^{\text{Pq}} = \gamma_{\text{pq}}$ , we see that Eqs. (39) and (40) correspond to a DAE model with the following effective direct exchange rates:

$$\gamma_{\alpha h}^{\text{eff}} = \gamma_{\alpha v} \gamma_{h v} \nu(t); \quad \gamma_{\alpha \beta}^{\text{eff}} = \gamma_{\alpha v} \gamma_{\beta v} \nu(t). \quad (41)$$

Note that the effective DAE rates (41) are by a factor  $c_v$  smaller than the vacancy exchange rates  $\gamma_{\text{pv}}$ .

Let us now consider more realistic VME models with the configuration-dependent saddle-point energies when correlators  $b_{ij}^{\text{p}}$  in (17) for different  $\text{p}$  are different. For such models, the basic adiabaticity equation (34) for vacancy activities  $\xi_i^v$ , generally, can not be solved analytically, thus either numerical or some approximate analytical methods should be used. Let us discuss two such approximate methods employed below. For a binary alloy, we can rewrite Eq. (34) in the form:

$$\sum_{j_{\text{nn}}(i)} b_{ij}^h \xi_i^v \xi_j^v \gamma_{h v} \left[ \left(1 + \eta_i r_{ij}\right) / \xi_i^v - \left(1 + \eta_j r_{ij}\right) / \xi_j^v \right] = 0 \quad (42)$$

where  $\eta_i = \eta_i^\alpha = \exp(\beta \lambda_i)$ , and  $r_{ij}$  is  $\gamma_{\alpha v} b_{ij}^\alpha / \gamma_{h v} b_{ij}^h$ . Eq. (42) can be approximately solved if products  $r_{ij} \eta_i^\alpha$  obey either of two inequalities:

$$\begin{aligned} \text{(a)} \quad \eta_i r_{ij} &= \exp(\beta \lambda_i) \gamma_{\alpha v} b_{ij}^\alpha / \gamma_{h v} b_{ij}^h \ll 1; \\ \text{(b)} \quad \eta_i r_{ij} &= \exp(\beta \lambda_i) \gamma_{\alpha v} b_{ij}^\alpha / \gamma_{h v} b_{ij}^h \gg 1. \end{aligned} \quad (43)$$

In the case (a), the second terms in round brackets in (42) are just small corrections to the first ones. In the zeroth approximation they can be neglected, thus the zero-order solution of Eq. (42) is:

$$\xi_i^v(i) = \nu(t) \gamma_{h v} \quad (44)$$

where the constant factor  $\gamma_{h v}$  is introduced so that the function  $\nu(t)$  is analogous to that in (36). Substituting (44) into (12), we again obtain Eqs. (37) or (38) for a binary alloy:

$$dc_i/dt = \sum_{j_{\text{nn}}(i)} M_{ij} 2 \sinh[\beta(\lambda_j - \lambda_i)/2]. \quad (45)$$

Here index "ah" at the effective mobility  $M_{ij}^{\alpha h} = M_{ij}$  is omitted for brevity, the expression for this mobility is similar to that in Eq. (39):

$$M_{ij}(\text{a}) = \gamma_{\alpha h}^{\text{eff}} b_{ij}^\alpha \exp[\beta(\lambda_i + \lambda_j)/2], \quad (46)$$

and  $\gamma_{\alpha h}^{\text{eff}}$  is the same as in (41).

In the case (b), we can rewrite Eq. (42) as:

$$\sum_{j_{\text{nn}}(i)} b_{ij}^\alpha \xi_i^v \xi_j^v \gamma_{\alpha v} \left[ \left(\eta_i + r_{ij}^{-1}\right) / \xi_i^v - \left(\eta_j + r_{ij}^{-1}\right) / \xi_j^v \right] = 0 \quad (47)$$

where the second terms in round brackets are again small corrections to the first ones. Thus the zero-order solution of this equation can be written as:  $\xi_i^{v(0)} = \nu(t) \gamma_{\alpha v} \eta_i$ , while corrections are proportional to  $r_{ij}^{-1}$ . However, taking into account these corrections is necessary to obtain a non-zero right-hand side of Eq. (12). In finding these small corrections, we can employ the approximation of a "smooth distribution of local concentrations" used to proceed from Eq. (28) to (30), that is, we can suppose the  $r_{ij}$  values for all bonds  $ij$  of the given site  $i$  to be close to each other:

$$r_{ij} \simeq r_{ii} \simeq r_{jj}. \quad (48)$$

Then the solution of Eq. (47) with the first-order corrections is provided by the relation:

$$\xi_i^v = \nu(t) \gamma_{\alpha v} \left( \eta_i + r_{ij}^{-1} \right). \quad (49)$$

Substituting (49) into (12) we again obtain Eq. (45) but correlator  $b_{ij}^\alpha$  in the effective mobility (46) is replaced by  $b_{ij}^h$ :

$$M_{ij}(\text{b}) = \gamma_{\alpha h}^{\text{eff}} b_{ij}^h \exp[\beta(\lambda_i + \lambda_j)/2]. \quad (50)$$

Physically, the opportunity to reduce the vacancy-mediated kinetics to the equivalent direct exchange kinetics is connected with the above-mentioned fact that in the course of evolution of an alloy, the distribution of vacancies adiabatically fast follows that of the main components. Therefore, one may suppose that such equivalence holds not only for simplified models (36) or (43), but is actually a general feature of the vacancy-mediated kinetics, while for more general models, correlators  $b_{ij}$ ,  $b_{ij}^\alpha$  or  $b_{ij}^h$  in Eqs. (39), (46) or (50) are probably replaced by some more complex expressions with similar properties.

Function  $\nu(t)$  in Eq. (41) determines the rescaling of time between the initial VME model and the equivalent DAE model (45). Temporal evolution of this DAE model is actually described by the "reduced time"  $t_r$  related to the real time  $t$  by the following differential or integral relations:

$$dt_r = \gamma_{\alpha h}^{\text{eff}} dt = \gamma_{\alpha v} \gamma_{h v} \nu(t) dt; \quad t_r = \int_0^t \gamma_{\alpha h}^{\text{eff}}(t') dt'; \quad (51)$$

$$t = \int_0^{t_r} \tau_{\alpha h}^{\text{eff}}(t'_r) dt'_r \quad (52)$$

where  $\tau_{\alpha h}^{\text{eff}} = (\gamma_{\alpha h}^{\text{eff}})^{-1}$  has the meaning of the mean time of an atomic exchange  $\alpha \rightleftharpoons h$ , while the variable  $t_r$  has a meaning of an effective number of such atomic exchanges. This natural physical variable is used below in describing the SSA simulation results.

To find the “rescaling function”  $\nu(t)$  in Eqs. (36)-(52), one should, generally, compare the results of simulation of precipitation based on the DAE model (45) to those based on the initial VME model. BV made such comparison for some simplified model of spinodal decomposition, while below we estimate  $\nu(t)$  for several realistic models of Fe-Cu alloys using comparison to the KMCA results. Note that the problem of rescaling of time between the real physical time and the time units employed in the simulation method used, e. g., number of Monte Carlo steps in the KMCA, persists in all simulations of VME kinetics (see Sec. IV C below), and it strongly depends, in particular, on the boundary conditions for vacancies adopted in simulations. For example, BV used the “vacancy conservation” model, while in simulations [16, 17] and below, a possible creation of vacancies at various lattice defects (grain boundaries, dislocations, etc) is taken into account. Thus, the form of the function  $\nu(t)$  depends also on the kinetic model used for vacancies.

The results presented in Fig. 10 below show that temporal variations of  $\nu(t)$  can be rather sharp. These variations arise due to qualitative changes in the distribution of vacancies with respect to minority atoms related to the phenomenon of “vacancy trapping” at interfaces of precipitates discussed in detail by BV and by Soisson and Fu [17] (SF). The resulting excess of vacancies near growing or shrinking interfaces leads to an acceleration of effective exchange rates  $\gamma^{\text{eff}}$  with respect to the incubation stage when the precipitates are absent. It results in an increase of  $\gamma^{\text{eff}}(t)$  after beginning of nucleation, and when the vacancy trapping effect is strong, this increase can be very large, which is illustrated by Fig. 10 below. At the same time, after the nucleation stage is over, the degree of this trapping does not change significantly. Therefore, the function  $\nu(t)$  can be expected to be approximately constant before and after nucleation and to monotonously increase with  $t$  in the course of nucleation, as illustrated by Fig. 3 of BV for  $\nu(t)$  in their simplified model.

### III. MAIN EQUATIONS OF STOCHASTIC STATISTICAL APPROACH

#### A. Basic ideas of the classical theory of nucleation

Before to describe the SSA, it is convenient to remind the main ideas of the classical theory of nucleation (CTN) [1–4]. The CTN treats embryos of a new phase within the original metastable one as sufficiently large objects which arise due to thermodynamic fluctuations. The simplest version of the CTN considers the embryo as a homogeneous droplet characterized by its radius  $R$ , the interface energy  $\sigma$ , and the free energy gain (with respect to the original metastable phase) per unit volume,  $\Delta f$ . The excess free energy needed to form this embryo is:

$$F(R) = 4\pi R^2\sigma - (4\pi R^3/3)\Delta f. \quad (53)$$

One of basic notions of the CTN is the critical embryo that can grow with no further loss of the free energy and thus with no fluctuations. For the model (53), it corresponds to the maximum of  $F(R)$  with respect to  $R$ , thus the critical radius  $R_c$  and the nucleation barrier  $F_c = F(R_c)$  are:

$$R_c = 2\sigma/\Delta f, \quad F_c = 16\pi\sigma^3/3\Delta f^2, \quad (54)$$

while the probability of the critical fluctuation needed to create this embryo is estimated according to the thermodynamic fluctuation theory [1]:

$$W_c \sim \exp(-F_c/T) \sim \exp(-\text{const } \sigma^3/T\Delta f^2). \quad (55)$$

Cahn and Hilliard [27] used the Ginzburg-Landau-type free energy functional to allow for the diffuse character of the interface of the critical embryo, but their approach is valid only at high  $T \sim T_c$  and for large embryos when the discrete lattice effects can be neglected. Dobretsov and Vaks [28, 29] developed a quantitative approach to calculate thermodynamics of critical embryos which takes into account the discrete lattice effects and uses the PCA rather than the simple MFA. Some results of this approach are used below in Table II and Fig. 2.

For supercritical embryos with  $R > R_c$ , the CTN suggests fluctuation effects to be insignificant. Therefore, after completion of nucleation, the main type of microstructural evolution is growth of embryos due to the diffusional flux of minority atoms from the matrix. Later on, the evaporation-condensation (or Lifshits-Slyozov-Wagner - LSW) mechanism becomes dominant when the larger precipitates grow at the expense of smaller ones [2]. Therefore, according to the CTN, decomposition of metastable solid solutions should include four well-defined stages [4]: (i) the incubation stage that precedes formation of first critical and supercritical embryos; (ii) the nucleation stage during which the supercritical precipitate density  $d_s$  reaches its maximum value; (iii) the growth stage when the density  $d_s(t)$  remains approximately constant but sizes of precipitates grow, and (iv) the coarsening stage when the density  $d_s(t)$  decreases due to the LSW evaporation-condensation mechanism.

These CTN ideas were confirmed by KMC simulations of Soisson and Martin [4] (SM) for some simple alloy model for which critical sizes and nucleation barriers (estimated in Table II below) are rather large, see, e. g., Fig. 1 of SM. However, in this work we mainly consider more realistic models of Fe-Cu alloys described in Sec. IV for which nucleation barriers and critical sizes are not large. Fluctuation effects in such alloys will be shown below to be strong and important not only for the nucleation but also for the growth stage.

#### B. Stochastic kinetic equation and filtration of noise

The quasi-equilibrium kinetic equations (10), (38) and (45) determine evolution of mean occupations of sites due

to the average atomic fluxes across each bond. However, these averaged equations can describe only those kinetic processes in which the total free energy  $F_{tot}$  decreases [22, 23], while the nucleation process should be accompanied by a fluctuative increase of this  $F_{tot}$  needed to overcome nucleation barriers. Therefore, to describe this process, we should consider fluctuations of atomic fluxes. The stochastic statistical approach for taking into account such fluctuations was suggested by SPV [20]. In this section we present main equations of this approach while their refinements are described below in Sec. IV.

We consider a binary alloy for which QKE has the form (45). In the SSA, this QKE is replaced by the stochastic kinetic equation (SKE) which can be conveniently written in the finite difference form (for a short time interval  $\delta t$ ) given by Eq. (19) of SPV:

$$\delta c_i \equiv c_i(t + \delta t) - c_i(t) = \delta c_i^d + \sum_{j_{nn}(i)} \delta n_{ij}^f. \quad (56)$$

Here  $c_i$  is the occupation of site  $i$  averaged over some locally equilibrated vicinity of this site, and the “diffusional” term  $\delta c_i^d$  corresponds to the average atomic transfer to site  $i$  described by the right-hand side of the QKE (45):

$$\delta c_i^d \{c_k\} = \sum_{j_{nn}(i)} M_{ij} 2 \sinh[\beta(\lambda_j - \lambda_i)/2] \delta t. \quad (57)$$

The last term  $\delta n_{ij}^f$  in the SKE (56) is the fluctuative atomic transfer through the bond ( $ij$ ) which is described by the Langevin-noise-type method: each  $\delta n_{ij}^f$  is treated as a random quantity with the Gaussian probability distribution:

$$W(\delta n_{ij}^f) = A_{ij} \exp[-(\delta n_{ij}^f)^2 / 2D_{ij}] \quad (58)$$

where  $A_{ij}$  is the normalization constant, and the dispersion  $D_{ij}$  is the same as that for the actual fluctuative transfer  $\delta n_{ij}^f$ . This dispersion is related to the mobility  $M_{ij}$  and the time interval  $\delta t$  in Eq. (57) by the “fluctuation-dissipation” type relation (18) of SPV:

$$D_{ij} = \langle (\delta n_{ij}^f)^2 \rangle = 2M_{ij} \delta t. \quad (59)$$

Unlike standard applications of the Langevin-noise method to mechanical systems, for the non-uniform statistical systems under consideration Eqs. (56)–(59) should be supplemented by the “filtration of noise” procedure that eliminates the short-wave contributions to fluctuations  $\delta n_{ij}^f$ . As discussed in detail by SPV, these contributions to Eq. (45) have been already included in the diffusional term  $\delta c_i^d$  which is obtained by statistical averaging just over these short-wave fluctuations. It agrees with the fact that all quantities entering Eq. (56), including the mean site occupation  $c_i$ , site chemical potentials  $\lambda_i$ , and the diffusional term  $\delta c_i^d$ , have a physical meaning only within some locally equilibrated region

called in textbooks “a quasi-closed subsystem” [1] that contains a sufficiently large number of atoms. In other words, in our statistical description implying division of the whole non-uniform non-equilibrium alloy into locally equilibrated quasi-closed subsystems, we consider only “thermodynamic” fluctuations  $\delta n_{ij}^f$  which have approximately the same value (for all bonds  $ij$  of the given crystal orientation  $\alpha$ ) within each quasi-closed subsystem, while a non-zero fluctuative contribution to the total  $\delta c_i$  in (56) arises only due to a relatively weak non-uniformity of these fluctuations. Therefore, in the last term of Eq. (56), the full fluctuative transfer  $\delta n_{ij}^f$  should be replaced by its long-wave (or “coarse-grained”) part  $\delta n_{ij}^{fc}$ . The latter can be obtained by introducing a proper cut-off factor  $F_c(\mathbf{k})$  in the Fourier-component  $\delta n_{f\alpha}(\mathbf{k})$  of the full fluctuation  $\delta n_{ij}^f \equiv \delta n_{\alpha}^f(\mathbf{R}_{s\alpha})$  where  $\mathbf{R}_{s\alpha}$  denotes the position of the bond  $ij$  center in the appropriate crystal sublattice  $\alpha$  formed by these centers [20]:

$$\begin{aligned} \delta n_{\alpha}^{fc}(\mathbf{R}_{s\alpha}) &= \sum_{\mathbf{k}} \exp(-i\mathbf{k}\mathbf{R}_{s\alpha}) \delta n_{\alpha}^f(\mathbf{k}) F_c(\mathbf{k}) \\ \delta n_{\alpha}^f(\mathbf{k}) &= \frac{1}{N} \sum_{\mathbf{R}_{s\alpha}} \exp(i\mathbf{k}\mathbf{R}_{s\alpha}) \delta n_{\alpha}^f(\mathbf{R}_{s\alpha}) \end{aligned} \quad (60)$$

where  $N$  is the total number of lattice sites (or atoms) in the crystal. The cut-off factor  $F_c(\mathbf{k})$  can be taken in the simple Gaussian-like form which for the BCC lattice looks as follows:

$$F_c^{\text{BCC}}(\mathbf{k}) = \exp[-4g^2(1 - \cos \varphi_1 \cos \varphi_2 \cos \varphi_3)] \quad (61)$$

where  $\varphi_{\nu} = k_{\nu}a/2$ ;  $k_{\nu}$  is the vector  $\mathbf{k}$  component along the main crystal axis  $\nu$ ; and  $a$  is the BCC lattice constant.

At large  $g^2 \gg 1$ , the expression (61) is reduced to a Gaussian  $\exp(-k^2 l^2 / 2)$  with  $l = ga$ . Thus, the reduced length  $g = l/a$  characterizes the mean size of locally equilibrated quasi-closed subsystems. Generally, it is the characteristic length of uniformity of site chemical potentials  $\lambda_i$ , which for a single-phase state (before nucleation) coincides with the uniformity length for local concentrations  $c_i$ . Estimates of this size are discussed below in Sec. IV B.

## IV. MODELS AND METHODS OF SIMULATIONS

### A. Alloy models and states used for simulations

In the most of our simulations we use the first-principle microscopic model of Fe-Cu alloys suggested by SF [17] that describes well available thermodynamic and kinetic data for such alloys. This is the second-neighbor interaction model based on *ab initio* Density-Functional Theory calculations using SIESTA code. For this model, configurational interactions  $v_n$  for the  $n$ -th neighbors in (22),



FIG. 1: (color online). Calculated phase diagrams for the SF model (upper figure) and LBS model (lower figure) described in the text. Thick lines (red online) correspond to the pair cluster approximation (PCA), and thin lines (green online) correspond to the mean-field approximation (MFA); solid lines are binodals, and dashed lines are spinodals. Solid circles and chained line show the binodal and spinodal calculated using the CALPHAD expression for free energy of bcc Fe-Cu alloys taken from [11]. Triangles indicate the  $(c, T)$  states used for simulations.

kinetic interactions  $u_n^{\text{Cu}} \equiv u_n$  in (17), saddle-point energy parameters  $\Delta^{\text{P}}$  in (33), activation energies  $E_{ac}^{\text{PV}}$  in (14) (all in eV) and attempt frequencies  $\omega_{\text{pv}}$  in (14) (in  $\text{sec}^{-1}$ ) have the following values:

$$\begin{aligned} v_1 &= -0.121 + 0.182T, & v_2 &= -0.021 + 0.091T, \\ u_1 &= 0.127 - 0.091T, & u_2 &= 0.044 - 0.045T, \\ \Delta^{\text{Cu}} &= 0.05, & \Delta^{\text{Fe}} &= -0.03 \\ E_{ac}^{\text{CuV}} &= 0.438, & E_{ac}^{\text{FeV}} &= 0.698, \\ \omega_{\text{CuV}} &= 5 \cdot 10^{15}, & \omega_{\text{FeV}} &= 2 \cdot 10^{15}. \end{aligned} \quad (62)$$

Here the second terms in expressions for  $v_n$  and  $u_n$  describe phenomenologically the influence of anharmonic and magnetic effects. Our simulations for the SF model were mainly performed at concentration  $c = 0.0134$  and three temperatures  $T$ : 773, 713 and 663 K; these alloy states will be denoted as the SF-1, SF-2 and SF-3 state, respectively. In Tables I and II and in Sec. V we also present some results for the alloy state SF-4 that corresponds to  $c = 0.0197$  and  $T=773$  K.

We also employ two more models suggested by Le Bouar and Soisson [16] (LBS). Parameters of these models have been fitted to energies of configurations and vacancy migration barriers computed with the Embedded Atom Method potential by Ludwig et al. [30]. The model LBS-1 is the nearest-neighbor interaction model with the following parameter values (in the same units as in (62)):

$$\begin{aligned} \text{LBS-1:} \quad v_1 &= -0.20, & u_1 &= 0.155, \\ \Delta^{\text{Cu}} &= \Delta^{\text{Fe}} = 0, \\ E_{ac}^{\text{CuV}} &= 0.018, & E_{ac}^{\text{FeV}} &= 0.64, \\ \omega_{\text{CuV}} &= \omega_{\text{FeV}} = 5 \cdot 10^{15}. \end{aligned} \quad (63)$$

For the model LBS-2, all parameters are the same as in (63) except for the saddle-point-energy parameter  $\Delta^{\text{Fe}}$  which is:

$$\text{LBS-2:} \quad \Delta^{\text{Fe}} = -0.238 \quad (64)$$

Our simulations for these two models were performed at  $c=0.01$  and  $T=1000$  K, and these alloy states will be denoted as the LBS-1 and LBS-2 state, respectively.

Comparison of SF and LBS models discussed in [17] (a more detailed comparison is given in Ref.[31]) shows, that the SF model yields a lower solution energy of copper in BCC iron (which leads to the lower density and

larger sizes of nucleating precipitates), and the larger difference between vacancy formation energies in pure BCC iron and pure BCC copper (which leads to a stronger vacancy trapping in copper precipitates and to a higher mobility of precipitates). As discussed by SF, the LBS models describe Fe-Cu alloys less realistically than the SF model, but we will consider these LBS models for methodical reasons, to follow the influence of variations of interaction constants and saddle-point energy parameters on the precipitation kinetics.

Binodals and spinodals for the SF and LBS models calculated using the PCA, MFA and CALPHAD expressions for free energy are presented in Fig. 1 where we also show the alloy states used in our simulations. These states are chosen in the metastable region  $T_s(c) < T < T_b(c)$  or  $c_b(T) < c < c_s(T)$  (where index  $s$  or  $b$  corresponds to the spinodal or binodal) which corresponds to the nucleation and growth (NG) type of alloy decomposition. The degree of supersaturation for each of these states can be quantitatively characterized by the reduced supersaturation parameter  $s$  introduced in [29]:

$$s(c, T) = [c - c_b(T)] / [c_s(T) - c_b(T)]. \quad (65)$$

Values  $s < 1$  correspond to the NG, while  $s > 1$ , to the spinodal decomposition (SD) evolution type; for the alloy states studied, values of  $s$  are presented in Table I.

To appreciate accuracy of results presented in Fig. 1 we first note that the PCA fully takes into account the pairwise correlations of atomic positions and neglects only many-particle ones [26]. Therefore, in the dilute alloy limit  $c_i \rightarrow 0$ , the PCA expressions for thermodynamic potentials become exact. In particular, the free energy (24) in this limit takes the form

$$F_{\text{PCA}} \Big|_{c \rightarrow 0} = -\frac{1}{2} \sum_{ij} c_i c_j f_{ij}, \quad (66)$$

which is just the discrete lattice analogue of the first term in the virial expansion of the free energy in powers of density (in our case, in powers of  $c_i$ ) for the standard “weakly non-ideal gas” theory [1]. Thus, at low concentrations under consideration, we can expect the accuracy of all thermodynamic results of the PCA, including both binodals and spinodals, to be high, and for all thermodynamic calculations we use the PCA.

TABLE I. Alloy states used in our simulations.

Model	SF				LBS-1,2
$T$ , K	773	713	663	773	1000
$c$ , at%	1.34	1.34	1.34	1.97	1
$s$	0.285	0.352	0.425	0.426	0.459
Alloy state	SF-1	SF-2	SF-3	SF-4	LBS-1,2

FIG. 2: (color online). Concentration profiles  $\Delta c_i = c_i - c$  in the critical embryos for the alloy states studied. Different curves from top to bottom correspond to the state SM [4], SF-1, SF-2, SF-4, SF-3 and LBS, respectively.

Fig. 1 shows that at relatively low  $c$  and  $T$  values used in our simulations, the binodals calculated using the PCA, MFA or CALPHAD methods do virtually coincide with each other. At the same time, the CALPHAD or MFA-calculated spinodals  $c_s(T)$  exceed those found in the PCA (and thus, the exact ones) by about twice. It leads to a strong underestimating of the reduced supersaturation  $s(c, T)$ , which, in its turn, should result in drastic distortions of microstructural evolution. Therefore, as mentioned in Sec. I, using the phase-field type methods based on CALPHAD or MFA expressions for thermodynamic potentials can hardly provide an adequate description of alloy decomposition kinetics at low concentrations and temperatures under consideration.

Fig. 2 illustrates the structure of “thermodynamic” critical embryos for the alloy states studied. This structure was calculated by the method of Ref. [28] mentioned in Sec. III A with the use of the PCA. The figure shows, in particular, that the sizes of critical embryos in our problem are comparable to the host (BCC iron) lattice constant:  $a_{\text{Fe}} = 0.287$  nm. In Table II we present main characteristics of these critical embryos: the reduced nucleation barrier  $F_c/T$ , the mean radius of the embryo,  $R_c$ , the total excess of minority (copper) atoms in the embryo with respect to the initial state,  $\Delta N_c$ , and the total number of minority atoms in the embryo,  $N_c$ . The barrier  $F_c$  is calculated according to Eq. (4) in [29] (where it was denoted as  $\Delta\Omega_c$ ), while quantities  $R_c$ ,  $\Delta N_c$ , and  $N_c$  are defined by relations:

$$\begin{aligned} R_c^2 &= \sum_i r_i^2 (c_i - c) / \Delta N_c, & \Delta N_c &= \sum_i (c_i - c), \\ N_c &= \Delta N_c + c N_s^c. \end{aligned} \quad (67)$$

Here index  $i$  numbers the lattice sites,  $N_s^c$  is the total number of sites (atoms) in a precipitate, and the term  $c N_s^c$  describes the contribution to  $N_c$  of the “uniform background” minority atoms. For comparison, in Fig. 3 and Table II we present also the analogous results for the SM [4] alloy state which corresponds to the nearest-neighbor interaction  $v_1 < 0$ ,  $T = 0.4(-v_1)$ , and  $c = 0.03$ .

TABLE II. Parameters of “thermodynamic” critical embryos for the alloy states considered.

Alloy state	$s$	$F_c/T$	$R_c$ , nm	$\Delta N_c$	$N_c$
SM [4]	0.287	7.48	0.488	32.5	33.8
SF-1	0.285	4.38	0.417	13.3	14.3
SF-2	0.352	2.47	0.438	9.7	10.7
SF-3	0.425	1.36	0.468	7.2	8.2
SF-4	0.426	1.90	0.475	10.4	11.9
LBS-1,2	0.459	0.83	0.497	5.4	6.2

Let us now discuss the expressions for effective mobilities  $M_{ij}$  in Eq. (45). Model LBS-1 corresponds to the configuration-independent saddle-point energies for which correlators  $b_{ij}^p$  in (17) do not depend on the kind  $p$  of an atom. As mentioned in Sec. II C, for this case the adiabaticity equation (34) is solved analytically, and the effective mobility  $M_{ij} = M_{ij}^{\text{ah}}$  is given by Eq. (39).

For two other models, SF and LBS-2, the saddle-point energies depend on configurations. Thus the adiabaticity equation (34) can be approximately solved only if either of inequalities (43) is obeyed at  $c_i$  values significant for the kinetic process studied; for brevity we denote such  $c_i$  as  $c_s$ . Let us first consider NG-type processes for the SF model. The experience of our simulations for all models considered (illustrated by Figs. 20-22 below) shows that the “significant for NG” local concentrations  $c_s$  have usually the order  $c_s \sim 0.1$ . To estimate products  $\eta_i r_{ij}$  in Eqs. (43), we first consider the case when these  $c_s$  are small, thus both the functions  $\ln(1 - g_{ij} c_j) \sim \ln(1 - f_{ij} c_s)$  in Eq. (20) and  $(1 + \bar{c}_{ij} f^{\text{AP}})^6 \sim \exp[6 \ln(1 + c_s f^{\text{AP}})]$  in Eq. (33) can be expanded in powers of  $c_s$ . Substituting numerical values of parameters (62) into these expansions we obtain the following estimates of  $\xi_{ij} = \eta_i r_{ij}$  for the SF-1 and SF-3 states:

$$\xi_{ij}^{\text{SF-1}} \sim 20 c_s \exp(80 c_s), \quad \xi_{ij}^{\text{SF-3}} \sim 40 c_s \exp(160 c_s) \quad (68)$$

while for the SF-2 state, the  $\xi_{ij}$  value lies between these two estimates. For  $c_s \gtrsim 0.1$ , all these values much exceed unity. Therefore, inequality (b) in (43) is obeyed, and the QKE (45) with the effective mobility  $M_{ij}$  given by Eq. (50) can be used for all our SF states.

To estimate products  $\xi_{ij} = \eta_i r_{ij}$  in Eqs. (43) for the LBS-2 state, we again expand functions  $\ln(1 - g_{ij} c_j) \sim \ln(1 - f_{ij} c_s)$  in (20) and  $(1 + \bar{c}_{ij} f^{\text{AP}})^6 \sim \exp[6 \ln(1 + c_s f^{\text{AP}})]$  in (33) in powers of  $c_s$ . Substituting numerical values of parameters from Eqs. (63), we obtain in this case:

$$\eta_i r_{ij}^{\text{LBS-2}} \sim 1400 c_s \exp(-40 c_s). \quad (69)$$

At  $c_s$  between 0.01 and 0.1, the right-hand side (rhs) of this estimate is large, inequality (b) in (43) is obeyed, and Eq. (50) for the effective mobility  $M_{ij}$  can be used; at  $c_s \gtrsim 0.15$ , this rhs is small, and Eq. (46) for  $M_{ij}$  can be used; and at  $c_s$  between 0.1 and 0.15, the rhs is of the order of unity, thus neither of inequalities (43) is obeyed. Therefore, the equivalence of the VME kinetics to that for the DAE model (45) can not be formally proved for the LBS-2 state, and we made no the SSA simulations for this state. However, the above-mentioned remarks enable us to suggest that actually such equivalence probably exists, with the mobility  $M_{ij}$  in the QKE (45) smoothly varying between expression (50) for  $c_s < 0.1$  and expression (46) for  $c_s > 0.15$ . Then the precipitation kinetics for the LBS-2 state should be quite similar to that for the LBS-1 state differing only by replacing in Eq. (46) the factor  $b_{ij}^\alpha = b_{ij}$  for the LBS-1 state by some smaller factor varying between  $b_{ij}^h < b_{ij}$  at  $c_s < 0.1$  and  $b_{ij}^\alpha = b_{ij}$  at  $c_s > 0.15$ . It should correspond just to some slowing down of precipitation kinetics for the LBS-2 state with

respect to the LBS-1 state, and the KMCA results of LBS [16] seem to agree with these considerations.

To characterize strength of configurational (or “thermodynamic”) interactions  $v_n$  and kinetic interactions  $u_n$  for the alloy states considered, in Table III we present values of Mayer functions  $f_n^v$  and of analogous “kinetic” functions  $f_n^u$  defined by relations:

$$f_n^v = \exp(-\beta v_n) - 1, \quad f_n^u = \exp(\beta u_n) - 1, \quad (70)$$

as well as functions  $f_\Delta^p$  in Eq. (33). Functions  $f_n^v$  enter Eqs. (20)–(24) for site chemical potentials  $\lambda_i$  and the free energy  $F$ , while functions  $f_n^u$  and  $f_\Delta^p$  enter Eqs. (25)–(33), (39), (46) and 50) for correlators  $b_{ij}^p$  and effective mobilities  $M_{ij}$ . In Table III we also present expressions for correlators  $b_{ij}^{\text{Fe}}$  and for reduced effective mobilities  $M_{ij}^r = M_{ij}/\gamma_{\alpha h}^{\text{eff}}$  in Eqs. (39), (46) and (50) at small  $c_i \simeq \bar{c}_{ij} \lesssim 1/f_1^v$  which have been mentioned to be most significant for the NG-type processes.

TABLE III. Values of functions  $f_n^v$ ,  $f_n^u$ ,  $f_\Delta^p$  in Eqs. (70) and (33) and expressions for correlators  $b_{ij}^{\text{Fe}}$  and reduced effective mobilities  $M_{ij}^r = M_{ij}/\gamma_{\alpha h}^{\text{eff}}$  in Eqs. (39), (46) and (50) at small  $c_i \simeq \bar{c}_{ij} \lesssim 1/f_1^v$  for the alloy states studied.

Alloy state	$f_1^v$	$f_2^v$	$f_1^u$	$f_2^u$	$f_\Delta^{\text{Fe}}$	$f_\Delta^{\text{Cu}}$	$b_{ij}^{\text{Fe}}$	$M_{ij}^r$
SF-1	4.1	0.3	5.2	0.9	5.8	24	$\exp(81c_i)$	$\exp(47c_i)$
SF-2	4.9	0.3	6.3	1.0	7.0	33	$\exp(98c_i)$	$\exp(57c_i)$
SF-3	5.9	0.3	7.5	1.1	8.5	43	$\exp(118c_i)$	$\exp(69c_i)$
LBS-1	9.2	0	5.0	0	5.0	5.0	$\exp(71c_i)$	$\exp(-3c_i)$

Let us discuss the results presented in Table III. First, they show that both the thermodynamic and kinetic interactions for the alloy systems considered are rather strong: the  $f_1^v$ ,  $f_1^u$  and  $f_\Delta^p$  values much exceed unity. It again shows that the MFA or CALPHAD-type expressions for thermodynamic and kinetic parameters based on the approximations  $\beta v_n \ll 1$ ,  $\beta u_n \ll 1$  [21] can not be used to describe these alloy states. Second, the last column of Table III shows that the NG kinetics for the SF model should notably differ from that for the less realistic LBS-1 model. At small local concentrations  $c_i$  considered, the reduced mobility  $M_{ij}^r$  for the LBS-1 model is virtually a constant close to unity, while for the SF model it sharply rises with  $c_i$  and is typically very large. According to Eqs. (58) and (59), this mobility determines scale of fluctuative terms in the SKE (56). Therefore, we can expect the manifestations of fluctuation effects for the SF model to be much stronger than for the LBS-1

model. It agrees with the KMCA results presented below in Figs. 11-14.

### B. Estimating the local equilibrium length for the SSA

As discussed in Sec. III B, the reduced length  $l = ga$  in the SSA equations (60) and (61) characterizes sizes of locally equilibrium quasi-closed subsystems used in our statistical description of a nonequilibrium alloy. This length can not be chosen lower than the characteristic length of non-uniformity of local chemical potentials,  $l_{\text{nu}}$ , which for the nucleation processes has typically the same order of magnitude as the critical embryo size  $R_c$ , see, e. g., Figs. 20-22 below. The actual distribution of local equilibrium lengths  $l \lesssim l_{\text{nu}}$  in an alloy varies with both space and time; in particular, after creation of a super-

FIG. 3: Total number of precipitates that contain  $i \geq p$  copper atoms,  $N_p(t_r, g)$ , versus the reduced time  $t_r$  defined by Eq. (51) obtained in SSA simulations with different  $g$  for the SF-1 state. Frames (a), (b) and (c) correspond to  $g$  equal to 1.75, 1.65 and 1.55, while different curves from left to right in each frame correspond to  $p=10, 20, 40, 60$  and  $70$ , respectively.

critical precipitate, the degree of local equilibrium in the adjacent region should significantly increase with respect to other regions where such precipitates are not born yet.

For simplicity we will characterize the distribution of all local lengths  $l$  by a single spatially averaged parameter  $\bar{l} = ga$  where the reduced length  $g$ , generally, varies with the evolution time  $t$  or the reduced time  $t_r$  (51) used in the SSA. After completion of nucleation at some  $t_r = t_r^N$ , the alloy rapidly approaches the full two-phase equilibrium, and the length  $\bar{l}$  should become large. Then the cut-off parameter  $g = g(t_r)$  in Eq. (61) at  $t_r \gtrsim t_r^N$  should be large, too, fluctuative terms  $\delta n_f$  in (56) become small, and the SKE (56) transforms into the QKE (45) with no fluctuation terms.

To describe the above-discussed physical picture with the minimal number of model parameters, we approximated the time dependence  $g(t_r)$  by the following simplest expression:

$$\begin{aligned} t_r < t_r^N : \quad & g(t_r) = g_0 \\ t_r > t_r^N : \quad & g^2(t_r) = g_0^2 + (t_r - t_r^N)CD^{\text{eff}}. \end{aligned} \quad (71)$$

Here  $D^{\text{eff}}$  is the effective reduced diffusivity which for the direct-exchange model (45) can be estimated as  $D^{\text{eff}} \simeq \gamma_{\text{FeCu}}^{\text{eff}}$  [32, 33]; and  $C$  is a numerical factor, e. g.,  $C=2$  for the standard diffusion law. At  $C \sim 1$ , the evolution of microstructure was found to virtually not depend on the  $C$  value, and usually we put  $C=2$ .

The simple model (71) for  $g(t_r)$  includes an unphysical break at  $t_r = t_r^N$  which leads to the presence of analogous fictitious breaks in various characteristics of evolution, e. g., in Figs. 4-7, 9, 10 and 15. As mentioned, in reality the effective equilibrium length starts to increase immediately after beginning of nucleation, thus the function  $g(t_r) = \bar{l}/a$  monotonously increases with time with no breaks. Therefore, for a more realistic description, we should use for  $g(t_r)$  some other models which describe its continuous increase with  $t_r$  and the resulting smooth decrease of fluctuations in the course of both nucleation and growth stages. However, the experience of our simulations shows that at  $t_r$  not close to  $t_r^N$ , the main characteristics of microstructure, such as the density and sizes of supercritical precipitates, are not sensitive to the detailed form of  $g(t_r)$  provided the scale of this function is determined by the ‘‘maximum thermodynamic gain’’ principle described below. Thus, in this work we employ for  $g(t_r)$  the simplest form (71).

The parameter  $g_0$  in Eq. (71) can be estimated by two ways. First, it can be found by fitting the SSA simulation results for the evolution of density of precipitates

to the analogous KMCA results, for example, to those presented in Figs. 11-14 below. However, such ‘‘KMCA-based’’ estimates of  $g_0$  would restrict possible applications of the SSA by the models for which reliable KMCA results are available. To estimate  $g_0$  within the SSA, we can try to extend the second law of thermodynamics, that is, the principle of the free energy minimum with respect to all its free parameters valid for equilibrium systems, to the kinetic processes in non-equilibrium systems studied. To this end we note that the main characteristics of microstructure formed in the course of the nucleation process, such as the characteristic non-uniformity length  $l_{nu} \sim \bar{l}$  mentioned above, can be considered as ‘‘free’’ parameters of a nonequilibrium state analogous to ‘‘static’’ free parameters for equilibrium systems. Thus it seems natural to suggest that the kinetic path of evolution of this nonequilibrium state should correspond to the maximum thermodynamic gain, that is, to the maximum rate of decrease of free energy. This suggestion can extend the ‘‘excess entropy production’’ approach to thermodynamics of irreversible processes discussed by Prigogine and coworkers [34] to the kinetics of essentially non-uniform and non-equilibrium systems under consideration. Then the characteristic value  $l_{nu} \sim g_0 a$  can be estimated from the condition of the maximum thermodynamic gain in the course of the nucleation process, which in our model (71) corresponds to the minimum of the free energy  $F(g_0, t_r \lesssim t_r^N)$  with respect to  $g_0$ .

This maximum thermodynamic gain should evidently correspond to the formation of maximum number of large supercritical precipitates. At the same time, the density  $d_p$  of such precipitates sharply depends on the effective size  $\bar{l}$  of quasi-equilibrium systems for the nucleation process. When  $g = \bar{l}/a$  is too large, the fluctuations are too weak to overcome nucleation barriers, while when  $g$  is too small, the fluctuations are too strong to allow formation of large and steadily growing precipitates. Therefore, the dependences  $d_p(g)$  should have a pronounced maximum at some optimal  $g = g_0$ . These considerations are illustrated by Fig. 3 where we present temporal dependences of the total number of precipitates containing  $i \geq p$  copper atoms,  $N_p(t_r, g)$ , obtained in the SSA simulations with different  $g$ . The ‘‘end of nucleation’’ time  $t_r^N$  here and below is defined as the time of creation of the last ‘‘critical’’ precipitate with  $p \geq p_c$ , while these  $p_c$  values (which for SF alloy states are close to the  $N_c$  values in Table II) are estimated in Sec. V A. Such definition of  $t_r^N$  is somewhat arbitrary but it makes virtually no effect on the simulation results. For the evolution shown in frame 3a, the fluctuations seem to be too weak, thus the length  $\bar{l} = ga$  is too large. For frame 3c, the fluctuations are evidently too strong which leads to an unphysical evolution of large precipitates: they do not grow, in disagreement with the second law of thermodynamics; thus, the  $g$  value here is too small. Finally, for the evolution shown in frame 3b, the  $g$  value seems to be close to optimum.

In Figs. 4-7 we present temporal dependences of the

FIG. 4: (color online). Temporal dependence of the free energy per copper atom,  $F(t_r, g_0)$ , obtained in SSA simulations with different  $g_0$  for the SF-1 state. Curves 1, 2, 3, 4 and 5 (red, green, blue, purple and black online) correspond to  $g_0 = 1.55, 1.65, 1.7, 1.75$  and  $1.85$ , respectively.

FIG. 5: (color online). Same as in Fig. 4 but for the SF-2 state. Curves 1, 2, 3 and 4 (red, green, blue and purple online) correspond to  $g_0 = 1.6, 1.7, 1.8$  and  $1.9$ , respectively.

free energy per copper atom,  $F(t_r, g_0)$ , obtained in the SSA simulations with different  $g_0$  in Eq. (71). For definiteness, the initial state for these simulations was taken uniform:  $c_i(0) = c = \text{const}$ , thus the initial increase of  $F$  at  $t_r \lesssim 0.1 t_r^N$  is related just to switching-on fluctuations at  $t_r = 0$  and has no physical meaning. At  $t_r \simeq t_r^N$ , functions  $F(t_r, g_0)$  show the above-mentioned fictitious breaks due the analogous breaks in our model function  $g(t_r)$  in (71). However, at  $t_r$  not close to zero or to  $t_r^N$ , say at  $t_r \sim 0.5 t_r^N$ , functions  $F(t_r, g_0)$ , presented in Figs. 4-7 can be realistic. Therefore, the ‘‘optimal’’  $g_0$  value can be estimated from comparison of these functions at  $t_r \sim 0.5 t_r^N$  for different  $g_0$ .

Figs. 4-7 show that these functions have a distinct minimum at certain  $g_0$  for each alloy state considered. For the SF-1 state, this minimum corresponds to  $g_0$  equal to 1.65 or 1.7; for the SF-2 state, to  $g_0 = 1.7$  or 1.8; for the SF-3 and LBS-1 states, to  $g_0 = 1.9$  or 1.8. The first values seem to be a bit more appropriate, but using in simulations the second values changes results only slightly; it is illustrated below for the SF-2 model. Therefore, for the reduced length  $g_0$  in Eq. (71) we use the following values:

$$\begin{aligned} g_0^{\text{SF-1}} &= 1.65; & g_0^{\text{SF-2}} &= 1.7; \\ g_0^{\text{SF-3}} &= 1.9; & g_0^{\text{LBS-1}} &= 1.9. \end{aligned} \quad (72)$$

The minimum local equilibrium lengths  $l_0 = g_0 a$  for these  $g_0$  have the same order of magnitude as critical sizes  $R_c$  in Table II, in accordance with the considerations mentioned above.

Let us comment on the loss of validity of the SSA at low  $g$  which is manifested, in particular, in the above-mentioned unphysical results presented in frame 3c. This problem was discussed in detail by SPV [20] who noted that the statistical approach used, in particular, basic equations (9)-(13) that include averaging over locally equilibrated quasi-closed subsystems, imply their reduced size  $g$  to be not too small, so that they include a sufficiently large number of atoms, while site chemical potentials  $\lambda_i$  within these subsystems should obey the

FIG. 6: (color online). Same as in Fig. 4 but for the SF-3 state. Curves 1, 2, 3 and 4 (red, green, blue and purple online) correspond to  $g_0 = 1.8, 1.9, 2$  and  $2.1$ , respectively.

FIG. 7: (color online). Same as in Fig. 4 but for the LBS-1 state. Curves 1, 2, 3, 4 and 5 (red, green, purple, blue and black online) correspond to  $g_0 = 1.7, 1.8, 1.9, 2$  and  $2.1$ , respectively.

FIG. 8: (color online). Parameter of non-equilibrium (73) for the incubation stage observed in SSA simulations with different reduced lengths  $g$ . Circles and squares (red and black online) correspond to the SF-1 and LBS-1 state, respectively. Arrows indicate  $g_0$  values in Eqs. (72).

local equilibrium condition  $\lambda_i \simeq \text{const}$ . The scale of violations of this basic condition can be characterized by the ‘‘parameter of non-equilibrium’’  $J$  introduced by SPV:

$$J(g, t_r) = \frac{1}{N_b} \sum_{i,j} |\lambda_i - \lambda_j| / T \quad (73)$$

where  $N_b$  is the total number of the nearest-neighbor bonds  $\{ij\}$ , and the sum is taken over all such bonds in an alloy. In Fig. 8 we show the values of this parameter averaged over incubation stage,  $J_{\text{inc}}(g) = \langle J \rangle_{\text{inc}}$ ; for different alloy states, functions  $J_{\text{inc}}(g)$  are similar. At small  $g \lesssim 1.5$ , these functions start to sharply rise which reflects sharp violations of statistical equilibrium within too small quasi-closed subsystems. However, for  $g = g_0$  values presented in Eqs. (72), this parameter is still small:  $J_{\text{inc}}(g) \sim 0.1-0.15$ , thus employing the SSA seems to be justified.

In Fig. 9 we show temporal dependences of the nonequilibrium parameter (73) at first stages of evolution. As mentioned, breaks in curves  $J(t_r)$  at  $t_r = t_r^N$  are due to the similar breaks in our simple model (71), while for more realistic models mentioned above these breaks should be replaced by some smooth decrease of  $J(t_r)$  at  $t_r \gtrsim 0.5 t_r^N$ . The increase of  $J(t_r)$  after beginning of nucleation is related to arising of interfaces and spacial non-uniformities which lead to some additional, ‘‘non-uniform’’ contributions to differences  $|\lambda_i - \lambda_j|$  in Eq. (73).

### C. Methods of KMCA simulations

The KMCA used in this study is described in detail in Refs. [16, 17]. We just recall here the physical principles of the method, underlining the difference with the SSA. The KMC simulations follow the evolution of the atomic configuration in a simulation box of  $N = 64^3$  lattice sites containing Fe and Cu atoms and one vacancy, with periodic boundary conditions. At each Monte Carlo step, 8

FIG. 9: (color online). Parameter  $J(g, t_r)$  (73) observed in the SSA simulations with  $g = g_0$  from (72). Curves 1, 2, 3 and 4 (red, green, blue and purple online) correspond to the SF-1, SF-2, SF-3 and LBS-1 alloy state, respectively.

atom-vacancy exchanges between nearest-neighbor sites can occur in a BCC lattice, with the jump frequencies  $W_{ij}^{pv}$  given by Eq. (6). The activation energies are exactly computed for each local configuration, without using any mean-field approximation. One of these exchanges is chosen, using a pseudo-random generator, by means of a residence time algorithm [35]. The physical time of the Monte Carlo simulation is given by:

$$t_{MCS} = 1 / \sum_{j=1}^8 W_{ij}^{pv} \quad (74)$$

where the sum runs over the 8 possible jumps. This time must be rescaled to take into account the real vacancy concentration, which depends on the precipitation microstructure. If one assumes that the vacancy concentration remains at equilibrium in the different phases during all the precipitation, a convenient way to perform this time rescaling is :

$$t = t_{MCS} \frac{c_V^{MC}(\text{Fe})}{c_V^{eq}(\text{Fe})} \quad (75)$$

where  $c_V^{eq}(\text{Fe})$  is the equilibrium vacancy concentration in pure iron and  $c_V^{MC}(\text{Fe})$  is the vacancy concentration in the copper-free regions of the KMC simulation box [16, 17]. The number  $N_p$  of copper-rich precipitates and their average size  $\langle i \rangle$  (discussed in Sec. V A) are computed by considering only clusters which contain  $i \geq p$  copper atoms connected by at least one nearest-neighbor bond.

#### D. Methods of SSA simulations

All SSA simulations were performed in the cubic box containing  $N=2 \times (64)^3$  BCC lattice sites with periodic boundary conditions. In describing precipitates, the precipitate containing  $i \geq p$  copper atoms is defined as a set of adjacent sites  $i$  (connected by at least one bond) for which their mean occupations  $c_i$  exceed a certain cut-off value:  $c_i \geq c_{cut}$ , while this set contains not less than  $p$  copper atoms:

$$N_{Cu} = \sum_i c_i \geq p. \quad (76)$$

The choice of  $c_{cut}$  was found to be not essential, and for definiteness we took it the same as in experimental studies [7]:  $c_{cut} = 0.05$ .

In solving the SKE (56) with the diffusional term (57), we should take into account that this term is proportional to product of the generalized mobility  $M_{ij}$  and the factor  $2 \sinh[\beta(\lambda_i - \lambda_j)/2] \simeq \beta(\lambda_i - \lambda_j)$  describing a thermodynamic driving force, while mobilities  $M_{ij}$  given by Eqs. (46) or (50) are proportional to the correlator  $b_{ij}^\alpha$  or  $b_{ij}^h$  very sharply rising with the local concentrations  $c_i$ ; the latter is illustrated by Eq. (33) and by two last columns of table III. These very sharp dependences do

not allow us to use for solving the SKE the standard iterative methods, such as the Euler or Runge-Kutta ones: after several iterations, the product  $M_{ij}\beta(\lambda_i - \lambda_j)$  becomes so large that the time step needed to achieve a numerical stability gets too small for these algorithms can be used. On the other hand, there is no physical reason for the diffusional term to be too large, as the high mobility  $M_{ij}$  should lead to a very fast approaching the local equilibrium state at which local chemical potentials of adjacent sites,  $\lambda_i$  and  $\lambda_j$ , are very close to each other. Thus, in reality diffusional terms (57) remain to be reasonably small. The problem with application of standard iterative methods arises due to their discrete nature, thus numerical values of differences  $|\lambda_i - \lambda_j|$  can not catch up with a very fast increase of  $b_{ij}$ , and the fictitious increase of their product happens.

To overcome this methodical difficulty, in our iterative computations we put restrictions on  $b_{ij}$  setting it to not exceed a certain value  $b_{ij}^{max}$ :  $b_{ij} \leq b_{ij}^{max}$ . Then we made simulations with different  $b_{ij}^{max}$ , from smaller to larger ones, until all physically important characteristics of evolution, including the incubation and nucleation time,  $t_r^{inc}$  and  $t_r^N$ , and the maximum density of supercritical precipitates,  $d_s^{max}$ , ceased to significantly change under increase of  $b_{ij}^{max}$ . It happens at  $b_{ij}^{max} = 250$ , and this value was used in all our simulations. Actually, at  $b_{ij}^{max} = 500$ , the  $d_s^{max}$  values may be even lower than at  $b_{ij}^{max} = 250$  (while for  $b_{ij}^{max} < 250$ , they monotonously increase with  $b_{ij}^{max}$ ) but differences lie within statistical errors. After the nucleation stage is over and fluctuations are switched off according to model (71), values  $|\beta(\lambda_i - \lambda_j)|$  typically decrease by two orders of magnitude with respect to the nucleation stage. This allows us to significantly decrease the  $b_{ij}^{max}$ , usually up to  $b_{ij}^{max} = 10$ , and thus to increase the time-step in solving equations. Again we checked that using the same  $b_{ij}^{max}$  equal to 250 both before and after  $t_r^N$ , and reducing it at  $t_r > t_r^N$  up to  $b_{ij}^{max} = 10$ , lead to the same description of evolution. In our case, using the Runge-Kutta method does not provide any improvement of stability for the numerical solution of equations while it needs more calculations at each integration step, so in our simulations we used the more simple Euler method.

Finally, let us discuss the rescaling of the reduced time  $t_r$  used in the SSA to the physical time  $t$  determined by Eq. (52). In accordance with the remarks in the end of Sec. II C, we suppose the effective mean time of direct atomic exchanges,  $\tau_{ah}^{eff}$  in (52), to be constant before and after nucleation (that is, at both  $t_r < t_r^{inc}$  and  $t_r > t_r^N$ ), and to linearly vary with  $t_r$  in the course of nucleation:

$$\tau_{ah} = \begin{cases} a_1, & t_r < t_r^{inc}; \\ a_1 + (a_2 - a_1) \frac{(t_r - t_r^{inc})}{(t_r^N - t_r^{inc})}, & t_r^{inc} \leq t_r \leq t_r^N; \\ a_2, & t_r > t_r^N. \end{cases} \quad (77)$$

The constant  $a_1$  is the ratio of physical and reduced incubation times:  $a_1 = t_{inc}/t_r^{inc}$ , while the constant  $a_2$

FIG. 10: (color online). Temporal dependence of effective direct exchange rate  $\gamma_{\text{CuFe}}^{\text{eff}}$  in Eq. (41) estimated from comparison to the KMCA results as described in the text. Different curves from top to bottom correspond to the alloy states LBS-1, SF-1, SF-2 and SF-3, respectively. Arrows indicate the incubation time  $t_{\text{inc}}$ .

FIG. 11: (color online). Evolution of density of precipitates containing  $i \geq p$  copper atoms,  $d_p$  (left scale), and the total number of such precipitates within the KMC simulation box  $V_s^{\text{KMC}}$ ,  $N_p = N_p^{\text{KMC}}$  (right scale), for the SF-1 alloy state. For the SSA simulations with  $V_s^{\text{SSA}} = 2V_s^{\text{KMC}}$ , these  $N_p$  should be doubled:  $N_p^{\text{SSA}} = 2N_p$ . Solid lines from top to bottom (green, red, blue and purple online) correspond to the KMCA results for  $p=11, 15, 21$  and  $26$ , respectively, while symbols (circles, squares, triangles and crosses) show the analogous results obtained in another KMC run. Dashed line shows the SSA results for  $p = 15$ ,  $g_0 = 1.65$ .

can be estimated from the fit of the SSA simulation results to the evolution rate at the coarsening stage. Thus, model (77) includes only two parameters,  $t_{\text{inc}}$  and  $a_2$ , which can be estimated either from comparison to KMC simulations or from experiments.

In this work we use for such estimates the KMCA results described below. The resulting rescaling of time is presented in Fig. 10 as the dependence of effective direct exchange rates  $\gamma_{\text{ah}}^{\text{eff}}$  in Eq. (51) (to be abbreviated  $\gamma^{\text{eff}}$ ) on the physical time  $t$ ; this dependence has a more clear physical meaning than  $\tau_{\text{ah}}(t_r)$  in Eq. (77). The results presented in Fig. 10 and in analogous Fig. 3 of BV [22] clearly illustrate the decisive role of vacancy trapping for temporal dependences of effective direct exchange rates. For all models considered, these rates monotonously increase with the evolution time  $t$  which reflects the development of vacancy trapping in the course of precipitation. For the BV model, this trapping is relatively weak, thus  $\gamma^{\text{eff}}$  increases to the coarsening stage just by about twice. For the LBS model, the vacancy trapping is also not too pronounced (though stronger than for the BV model), thus the full increase of  $\gamma^{\text{eff}}$  is about 6 times. For the more realistic SF model, the vacancy trapping is very strong [17]. Thus for all three SF states considered, the  $\gamma^{\text{eff}}$  values rise between the incubation and nucleation stages by more than two orders of magnitude, and with lowering temperatures  $T$  this rise seems to increase, in accordance with a probable more strong trapping at lower  $T$ .

## V. EVOLUTION OF MICROSTRUCTURE OBSERVED IN KMCA AND SSA SIMULATIONS

### A. Evolution of density and sizes of precipitates

Evolution of density of different precipitates is shown in Figs. 11-14. Solid lines and symbols in these figures

FIG. 12: (color online). Same as in Fig. 11 but for the SF-2 state and  $p=8, 11, 16$  and  $21$ , respectively. Dashed curve shows the SSA results for  $p = 11$ ,  $g_0 = 1.7$ , and chained line, the SSA results for  $p = 11$ ,  $g_0 = 1.8$ .

FIG. 13: (color online). Same as in Fig. 11 but for the SF-3 state and  $p=6, 8, 11, 16$  and  $21$ , respectively, while dashed curve shows the SSA results for  $p = 8$ ,  $g_0 = 1.9$ .

show the results obtained in two different KMC runs; differences between these lines and symbols illustrate the scale of errors (mainly, statistical) of these KMC results. Fig. 11 shows that for the SF-1 state and relatively small precipitates,  $p \lesssim 10$ , such errors at the nucleation stage are significant. while at larger  $p$ , and at later stages of evolution, these errors decrease. For the LBS-1 model (Fig. 14), differences between two KMC runs are lower as the fluctuation effects here are much weaker. Let us also note that the difference between values of  $d_p$  at two neighboring curves,  $d_{p_1}(t)$  and  $d_{p_2}(t)$  in Figs. 11-14:  $d(i) = (d_{p_1} - d_{p_2})$ , has the meaning of the density of precipitates that include  $i$  copper atoms with  $i$  between  $p_1$  and  $p_2$ :  $p_1 \leq i < p_2$ .

Let us first discuss the KMCA results presented in Figs. 11-14. First, we note that they qualitatively agree with the classical theory nucleation (CTN) ideas described in Sec. III A. In particular, all dependences  $d_p(t)$  reveal presence of four main stages of decomposition: incubation, nucleation, growth and coarsening. For more quantitative comparison to the CTN, we should estimate the ‘‘critical’’ embryo size  $p_c$ . In thermodynamic calculations [27–29], the critical embryo is precisely defined as the set of mean occupations  $\{c_i\}$  that corresponds to the saddle-point of the generalized free energy  $F\{c_i\}$  in the multi-dimensional space  $c_i$  [28]. At the same time, for nucleating precipitates the analogous critical size can not be defined uniquely. It seems natural to define it as the lowest value of the embryo size  $p$  such that the most probable evolution path at  $p > p_c$  is growth rather than shrinkage or dissolution, but due to the presence of fluctuations inherent to the nucleation process, such ‘‘kinetic’’ critical sizes can be determined just approximately.

Using KMCA results presented in Figs. 11-14, we can estimate these  $p_c$  from the shape of curves  $d_p(t)$  at different  $p$ . For the SF model, for which fluctuations in dependences  $d_p(t)$  are pronounced at small  $p$  and decrease at larger  $p$ , we can suggest that beginning of decreasing these fluctuations with increasing  $p$  should correspond to the relation  $p \gtrsim p_c$ . For the states SF-1, SF-2 and SF-3, it corresponds to  $p_c \sim 15$ ,  $p_c \sim 11$ , and  $p_c \sim 8$ .

FIG. 14: (color online). Same as in Fig. 11 but for the LBS-1 state and  $p=6, 11, 15$  and  $26$ , respectively, while dashed curve shows the SSA results for  $p = 15$ ,  $g_0 = 1.9$ .

As these estimates agree well with the “thermodynamic” critical sizes  $N_c$  in Table II, we will use for the critical size  $p_c$  in the SF-1, SF-2 and SF-3 alloy state the value 15, 11 and 8, respectively. Note that in the SSA simulations, the  $p_c$  values are used only to define the “end of nucleation” time  $t_r^N$  in Eq. (71) as the time of creation of the last critical precipitate, and slight variations of  $p_c$  have almost no effect on evolution.

Figs. 11-13 show that temporal dependences  $d_p(t)$  at these  $p=p_c$  have, generally, a common form similar to that obtained by SM [4] for their simplified model that agrees with the CTN ideas described in Sec. III A. At the same time, these dependences reveal at least two differences from the CTN ideas.

(A) Fluctuations in dependences  $d_{p_c}(t)$  are rather pronounced and significant even for “supercritical” embryos with  $p > p_c$ , and the more so for undercritical ones with  $p < p_c$ . It is particularly clear seen for the KMC results presented in Fig. 11 by solid lines, while in Figs. 12 and 13 these fluctuations are partly smoothed due to the plotting of lesser number of the results.

(B) These fluctuations are large and important not only during nucleation but also after its completion when the average density of supercritical precipitates ceases to increase. It is seen, in particular, in Fig. 13 where curve  $d_p(t)$  at  $p = 16 \simeq 2p_c$  reveals a wide and pronounced minimum between  $t = 3 \cdot 10^5$  and  $4 \cdot 10^5$  sec falling here by about 1.5 times. Therefore, for the SF model, the fluctuations are important for evolution even at the growth stage.

Let us now discuss dependences  $d_p(t)$  for the LBS-1 state for which the thermodynamic nucleation barrier  $F_c$  (given in Table II) is low:  $F_c \lesssim T$ . In this case, evolution of not large “thermodynamically supercritical” embryos with  $p \gtrsim N_c$  again differs from the CTN ideas: effects of fluctuations here are strong due to the low thermodynamic gain under growth of such embryos. As their stability is low, they often dissolve rather than steadily grow as the CTN supposes. It can qualitatively explain a significant decrease of “plateau” in curves  $d_p(t)$  with  $p \geq 15$  as compared to  $p=6$  and  $p=10$  in Fig. 14. For this case, it seems more adequate to suppose the kinetic critical size  $p_c$  to significantly exceed  $N_c$ , so that the dominant evolution path at  $p > p_c$  would be growth of the embryo. For the LBS-1 state, we estimate this size as  $p_c \simeq 15$ .

The SSA results for the precipitate density  $d_p(t)$  presented in Figs. 11-14 have been obtained as described in Sec. IV. Note that rescaling of time  $t_r$  used in the SSA to the time  $t$  used in the KMCA (illustrated by Fig. 10) corresponds to the above-described two-parametric fit of only “horizontal” intervals in Figs. 11-14, while “vertical” intervals, that is, the density  $d_p$  values, are calculated in the SSA with no adjustable parameters. We see that for all four alloy states considered, these  $d_p(t)$  agree with the KMCA results within errors of these results mentioned above. Fig. 12 (as well as frame 15b below) also shows that changes in the SSA results due

FIG. 15: (color online). Average number of copper atoms within a precipitate,  $\langle i \rangle$ , versus the evolution time  $t$  (in seconds). Frames *a*, *b*, *c* and *d* correspond to the alloy states SF-1, SF-2, SF-3 and LBS-1, respectively. Solid lines and squares correspond to the KMCA. Dashed lines correspond to the SSA with  $g_0$  from (72), and chained line (in frame *b*), to  $g_0=1.8$ . Arrows show the values of  $t$  that correspond to  $t_r^N$  in Eq. (71).

FIG. 16: (color online). Upper frame: Distribution of copper atoms for the SF-1 alloy state just before nucleation,  $t=55$  sec., observed in the KMCA. Each sphere (blue online) corresponds to a copper atom. Lower frame: Distribution of local concentrations  $c_i$  for the same state as in the upper frame observed in the SSA. Relation between coloring and  $c_i$  value on the lattice site  $i$  is shown in the right part of the frame. Sites with  $c_i < 0.05$  are not shown.

to possible variations of  $g_0$  between  $g_0=1.7$  and  $g_0=1.8$  mentioned in derivations of estimates (72) are relatively small.

In Fig. 15 we show temporal dependences of average number of copper atoms within a precipitate (“precipitate size”)  $\langle i \rangle = i_p(t)$ . Results of the KMCA and SSA calculations seem usually to agree within the KMCA errors except for time intervals just after  $t_r^N$  where  $i_p^{\text{SSA}}$  notably exceed  $i_p^{\text{KMCA}}$ . This disagreement seems to be again related to crudeness of the oversimplified model (71) for the length  $g(t_r)$  determining scale of fluctuative terms  $\delta n_f$  in the stochastic equation (56). As mentioned, model (71) corresponds to the constant  $g(t_r) = g_0$  at  $t_r < t_r^N$  and to a sharp increase of  $g$  (and thus to practically abrupt switching-off fluctuations) at  $t_r \geq t_r^N$ , while actually the length  $g$  starts to increase (and fluctuations  $\delta n_f$  to decrease) immediately after beginning of nucleation, and  $g$  remains to be finite (and nucleation effects to be noticeable) at the growth stage, too. Thus at  $t_r > t_r^N$ , the SSA-calculated  $i_p(t)$  in Fig. 15 grow more rapidly than in the KMCA (and in reality) as actually this growth is still hampered by noticeable fluctuation effects. Therefore, we can expect that these disagreements will be reduced or vanished if the models of  $g(t_r)$  more realistic than (71) will be used in the SSA.

## B. Features of microstructure at different stages of precipitation

In Figs. 16-19 we show microstructure of the SF-1 alloy state at different stages of evolution observed in the KMCA and SSA-based simulations. As the SSA simula-

FIG. 17: (color online). Same as in Fig. 16 but at the end of nucleation,  $t=1000$  sec. Light spheres (yellow online) in the upper frame show copper atoms that belong to some supercritical precipitate.



FIG. 18: (color online). Same as in Fig. 17 but at the beginning of coarsening,  $t=2000$  sec.

FIG. 19: (color online). Same as in Fig. 17 but at some intermediate stage of coarsening,  $t=4000$  sec.

tion box was twice as large as that used in the KMCA, the total number of precipitates in the SSA-based (lower) frame of each of Figs. 16-19 exceeds that presented in the KMC-based (upper) frame by about twice. Figs. 16-19 illustrate processes of nucleation, growth and coarsening discussed above.

In comparison of the KMCA and SSA results in Figs. 16-19 we note that the SSA, as well as any other statistical description, disregards details of particular atomic configurations presented in the KMCA snapshots, but it enables us to pick out essential features of microstructure which often can not be easily apprehended in these snapshots. It is illustrated by Fig. 16 where the SSA frame clearly shows a number of regions significantly enriched by copper atoms, that is, precursors of precipitates to be created, while such regions are not clearly seen in the analogous KMC frame. Similar differences in describing precipitates can be seen in Figs. 17-19. Main quantitative characteristics of precipitates, such as their density and sizes discussed above, can be easily determined in both approaches. At the same time, the presence of significant crystalline anisotropy, particularly for not large precipitates, in the KMCA can be established only after some special analysis [15, 17], while in the SSA frames it is seen at first sight. Difference between two descriptions is also evident for interfaces of precipitates. In the KMCA frames of Figs. 17-19, these interfaces are usually rather sharp but typically not flat and not regular, while in the analogous SSA frames, these interfaces seem to be somewhat diffuse and have typically “intermediate” values of local concentration:  $c_i \sim 0.5$  (green online). The differences arise because each local concentration  $c_i$  in the SSA is obtained by averaging over some locally equilibrated vicinity of site  $i$ , that is, over a relatively rapid motion of surface atoms on the “not-filled” facet considered. At the same time, inner parts of precipitates (for both the KMCA and SSA) include only copper atoms which in the SSA frames is clearly seen on cuts of precipitates by the boundary planes of simulation box.

Therefore, Figs. 16-19 also illustrate a complementary character of describing evolution of microstructure by the KMCA and the SSA.

### C. Kinetics of nucleation

As discussed above, the SSA provides a partly averaged description of atomic distributions aiming mainly at adequate calculations of locally averaged quantities, such as the density of different precipitates, their structure,

FIG. 20: (color online). Distribution of local concentrations within a plane containing several nucleating precipitates for the SF-1 state at the following reduced time  $t_r$  values: (a) 7.5, (b) 7.9, (c) 8.0, (d) 6.1, (e) 8.5, and (f) 9.0. For each point  $\mathbf{r}$  of the figure, the  $c(\mathbf{r})$  value is obtained by interpolation between  $c_i$  on neighboring lattice sites. Relation between coloring and  $c_i$  values is shown in the right part of the figure.

morphology, etc. Therefore, quantitative treatments of phenomena which are mainly determined by fluctuations, such as processes of creation and evolution of undercritical and near-critical embryos, lies, generally, outside the scope of the SSA. However, as mentioned above, the qualitative changes of microstructure, such as those corresponding to the nucleation process, can often be more easily followed in the SSA rather than in the KMCA. Therefore, it can be instructive to study kinetic details of nucleation with the use of the SSA, even though the scale of fluctuation effects in such study is most probably underestimated.

Some results of such studies are presented in Figs. 20-22 which illustrate processes of sequent creation of three supercritical embryos for the SF-1 alloy state. Frames 20a-20e also show processes of creation and dissolution of an “undercritical” embryo: the concentration fluctuation in the right central part of these frames first increases up to the values  $c_i \sim 0.1$ , but then decreases and disappears. On the contrary, frames 20d-20f illustrate a “successful” nucleation process. The local fluctuation below that discussed above first increases in both size and amplitude, and then suddenly shrinks with formation of a “kinetic” supercritical embryo. Later on this embryo survives and grows, but this growth is first non-monotonic and includes a “partial dissolution” process illustrated by frames 21a and 21b. Note that at first stages of this process shown in frames 20e and 20f, the embryo is extended and shapeless, while later on it is rather wrong-shaped, thus it seems to have little in common with the “thermodynamic” critical embryos shown in Fig. 2.

Creation and evolution of two other embryos shown in Figs. 21 and 22 proceeds similarly. In both cases, the initial extended and shapeless fluctuation of concentration first suddenly shrinks so that maximum concentrations within it reach “critical” values  $c_i \gtrsim 0.12$ , after which embryos seem to become “supercritical”. Then subsequent fluctuations lead to a partial dissolution of these embryos, but in both cases they survive and later on start to grow. This growth correspond to “sucking” of copper atoms from adjacent regions and thus to depletion of copper concentration in these regions.

The examples considered can also illustrate the kinetic mechanism of nucleation. It can be viewed as a local spinodal decomposition that starts when the amplitudes and extension of local fluctuative enrichment of concentration become large enough in order that the “uphill

FIG. 21: (color online). Same as in Fig. 20 but at the following  $t_r$ : (a) 21, (b) 24, (c) 29, (d) 31, (e) 34, and (f) 38.

FIG. 22: (color online). Same as in Fig. 20 but at the following  $t_r$ : (a) 46, (b) 47, (c) 48, (d) 49, (e) 50, and (f) 53.

diffusion” mechanism characteristic of spinodal decomposition [32] becomes operative. For the examples considered, it seems to correspond to local concentrations  $c_i \gtrsim 0.07-0.09$  (while the uniform spinodal decomposition boundary, according to Fig.1, is  $c_s \simeq 0.045$ ) in the region  $l \gtrsim (7-8)a$ . Such interpretation of nucleation as a fluctuation-induced local spinodal decomposition can be useful for qualitative understanding of many phenomena in this field, in particular, of a great excess in probabilities of nucleation near the binodal curve observed experimentally [36] with respect to estimates of the classical theory of nucleation (55).

#### D. Changes in microstructural evolution under variations of temperature or concentration

As mentioned in Sec. IV A, the kinetic type of alloy decomposition is mainly determined by the value of the reduced supersaturation  $s$  (65), which for metastable states under consideration is less than unity. Low  $s$  correspond to the states with the concentration and temperature ( $c, T$ ) values close to the binodal curve for which a “deep NG” type of evolution with a low density and large sizes of nucleating precipitates is characteristic. An increase of  $s$  corresponds to approaching the spinodal curve and decreasing nucleation barriers, thus nucleating precipitates should become smaller (which is illustrated by Table II), while their density should increase. Basing on these considerations, we can expect that the reduced supersaturation  $s$  is the main parameter determining microstructural evolution, but at the given  $s$ , microstructure can also significantly vary with the concentration or temperature.

To get an idea about these variations, in Fig. 23 we show microstructure at the end of nucleation for the SF-1, SF-3 and SF-4 alloy states described by Tables I, II and Fig. 2. In simulations for the SF-4 state (which has the same supersaturation as the SF-3 state but higher concentration and temperature) we used  $g_0 = 1.9$  value, same as for the SF-3 state. In accordance with considerations mentioned above, the increase of supersaturation  $s$  in states SF-3 and SF-4 with respect to SF-1 by about

FIG. 23: (color online). Distribution of concentrations  $c_i$  at the end of nucleation for the following alloy states: (a) SF-1, (b) SF-3, and (c) SF-4.

1.5 times leads to much higher density of nucleated precipitates: by about 3.6 times for the SF-3 state, and by 2.2 times for the SF-4 state. At the same time, frames 23b and 23c illustrate differences in microstructure for the same  $s$  but different  $c$  and  $T$ . For the state SF-4, precipitates are notably larger while their density is by 1.5 times lower than those for the state SF-3. These differences can be qualitatively explained by the differences in characteristics of thermodynamic critical embryos for these two states presented in Table II and Fig. 2: both critical sizes and reduced nucleation barrier  $F_c/T$  and for the SF-4 state notably exceed those for the SF-3 state.

## VI. CONCLUSIONS

To conclude, we summarize the main results of this work.

1. The consistent and computationally efficient stochastic statistical approach is developed to microscopically study kinetics of decomposition of metastable alloys.

2. In this approach, description of evolution in terms of certain reduced time includes no adjustable parameters. Rescaling of this reduced time to the physical time can usually be made with the use of few constants which can be estimated either from comparison to kinetic Monte Carlo simulations or from experiments.

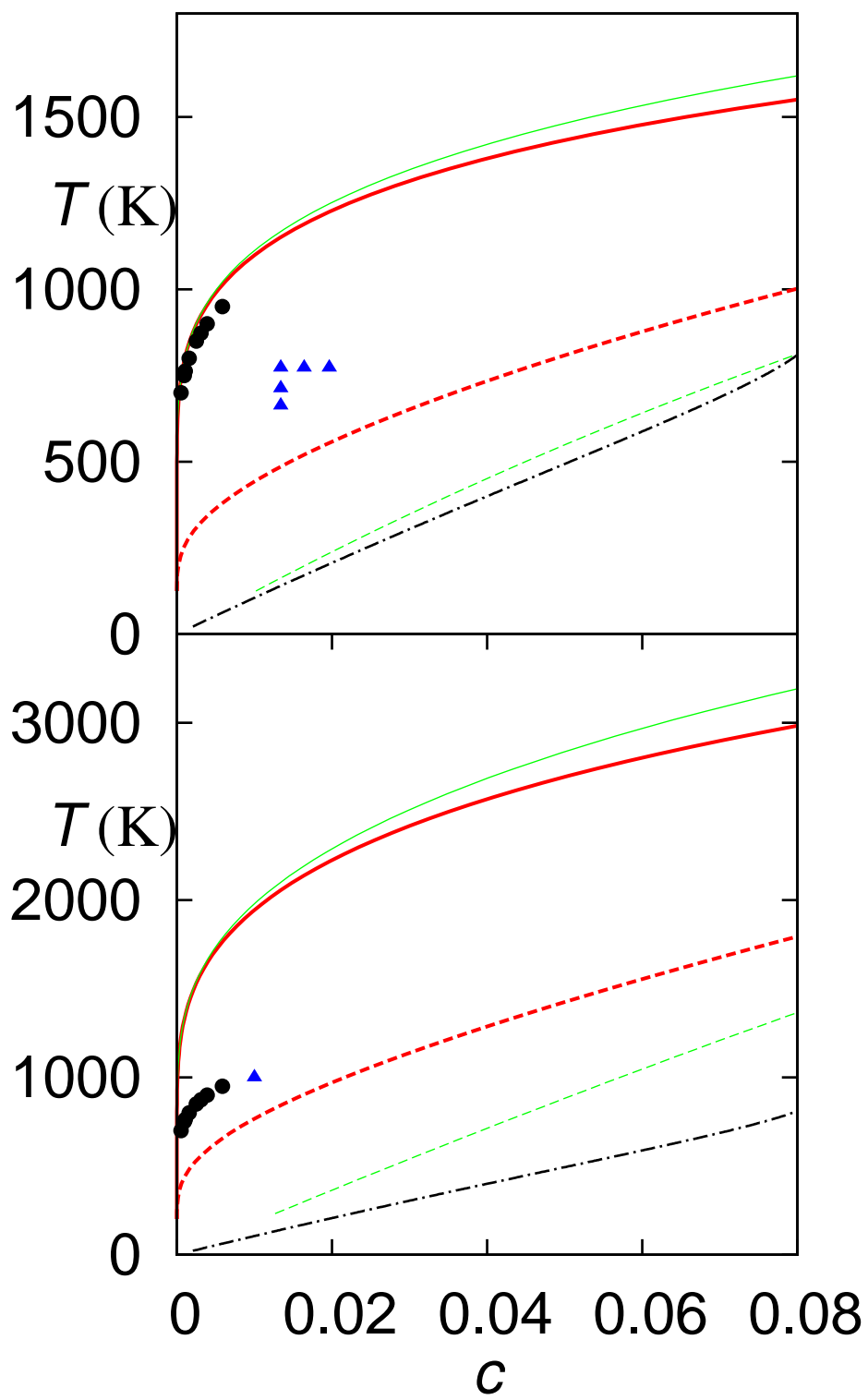
3. For several realistic models of iron-copper alloys studied, the results of this approach usually agree with the kinetic Monte Carlo simulation results within errors of these simulations.

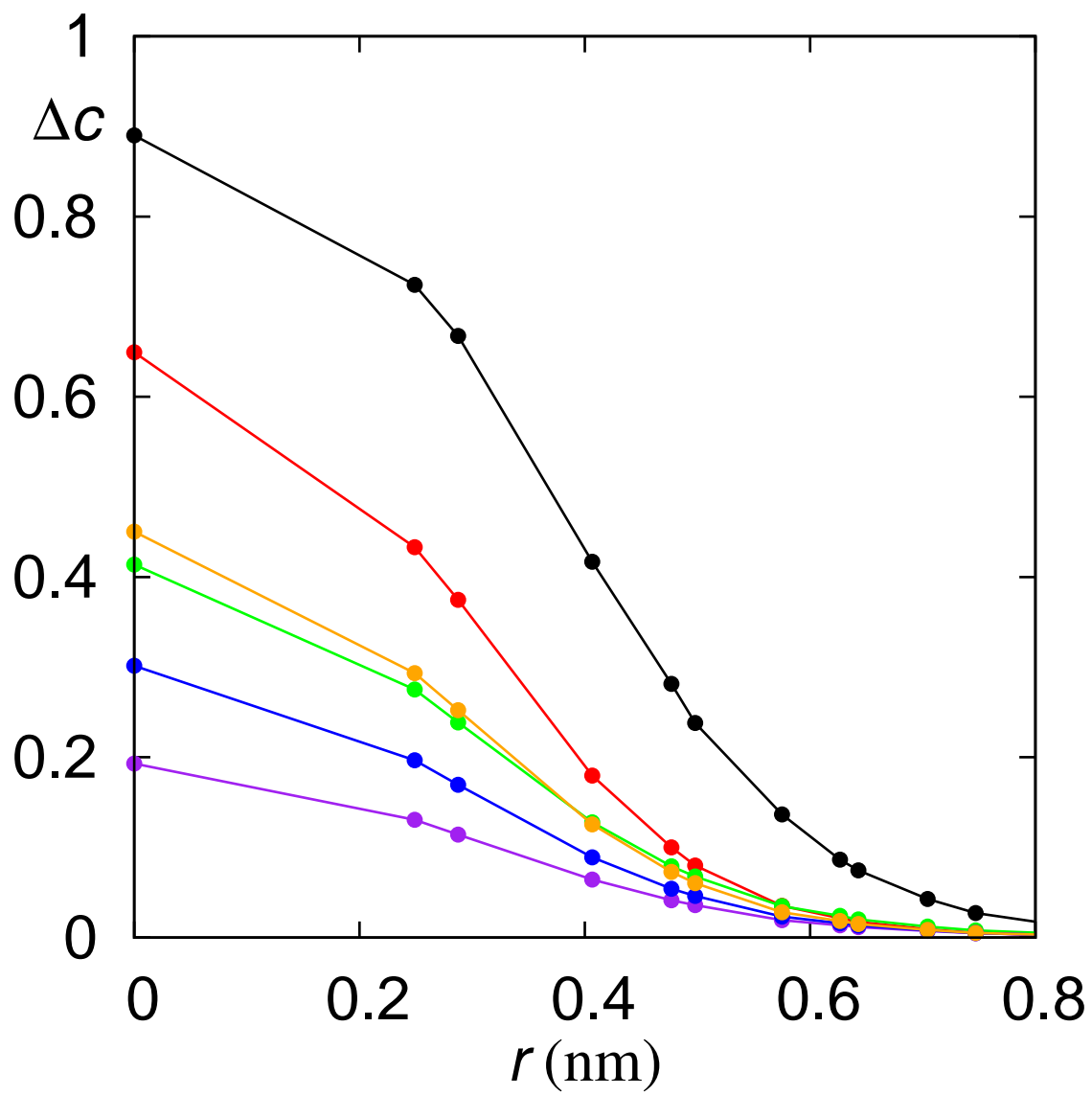
4. Oversimplified model (71) for the important kinetic parameter of the theory, size of locally equilibrated regions, seems to be sufficient for describing main characteristics of microstructure. However, for an adequate description of temporal dependences we should use more realistic models discussed in Secs. IV B and V A.

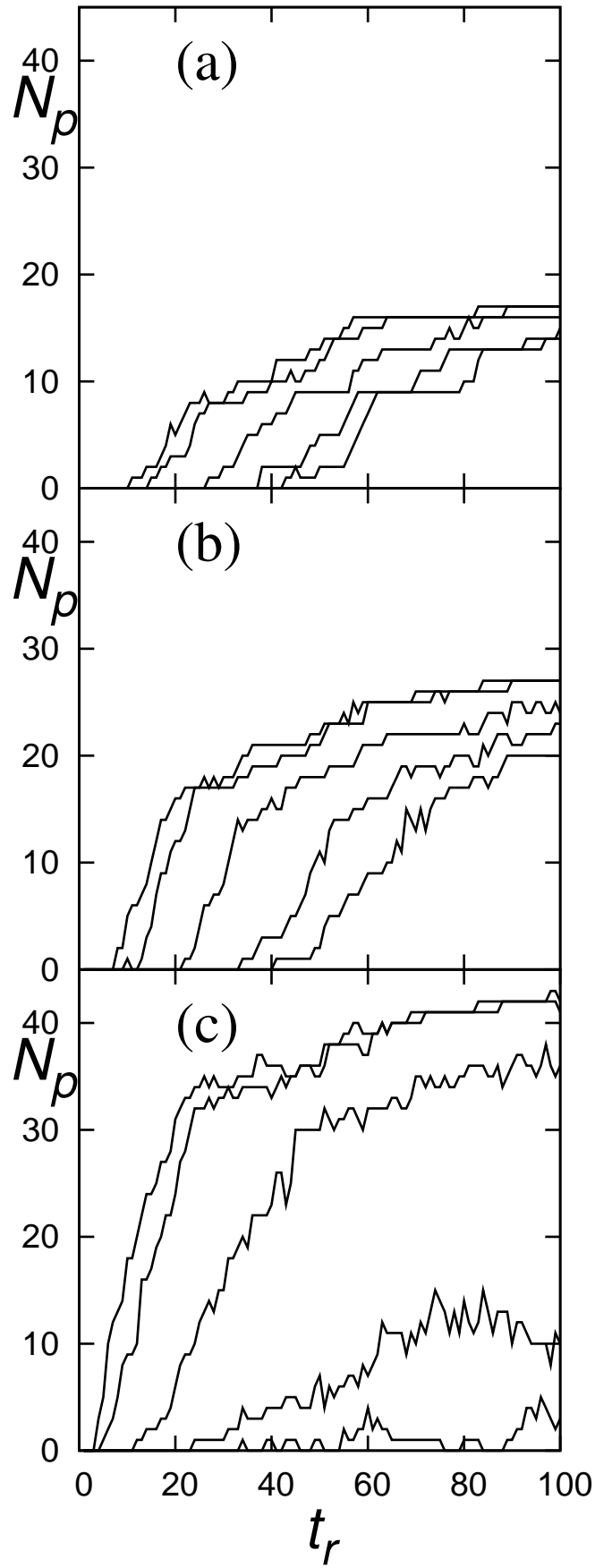
## ACKNOWLEDGMENTS

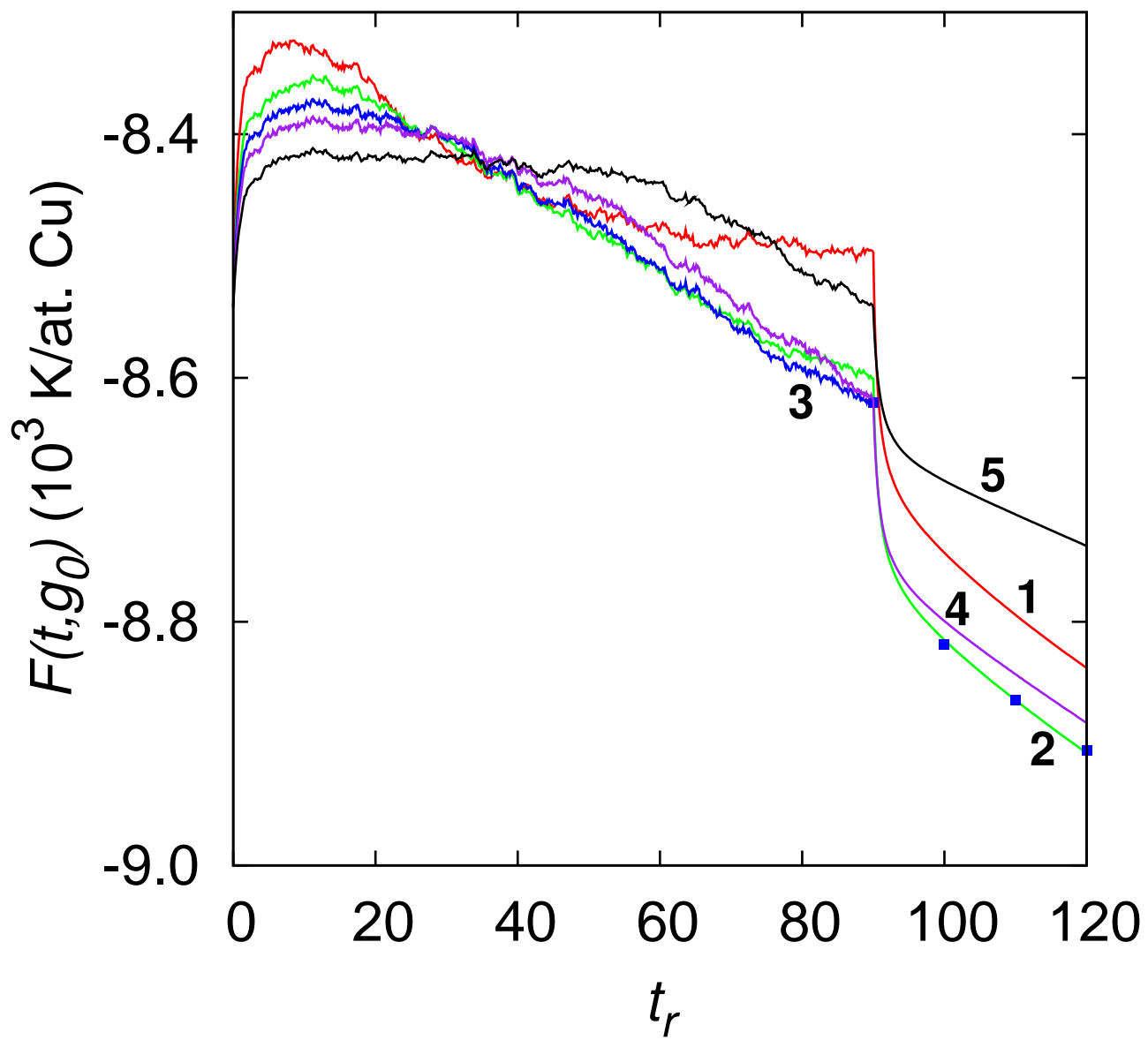
The authors are much indebted to I.A. Zhuravlev for his help in this work, as well as to Yu. N. Gornostyrev, P. A. Korzhavy and Georges Martin, for numerous valuable discussions. The work was supported by the Research Technological Center “Ausferr”, Magnitogorsk, by the Russian Fund of Basic Research (grant No. 06-02-16476); by the fund for support of leading scientific schools of Russia (grant No. NS-3004.2008.2); and by the program of Russian university scientific potential development (grant No. 2.1.1/4540).

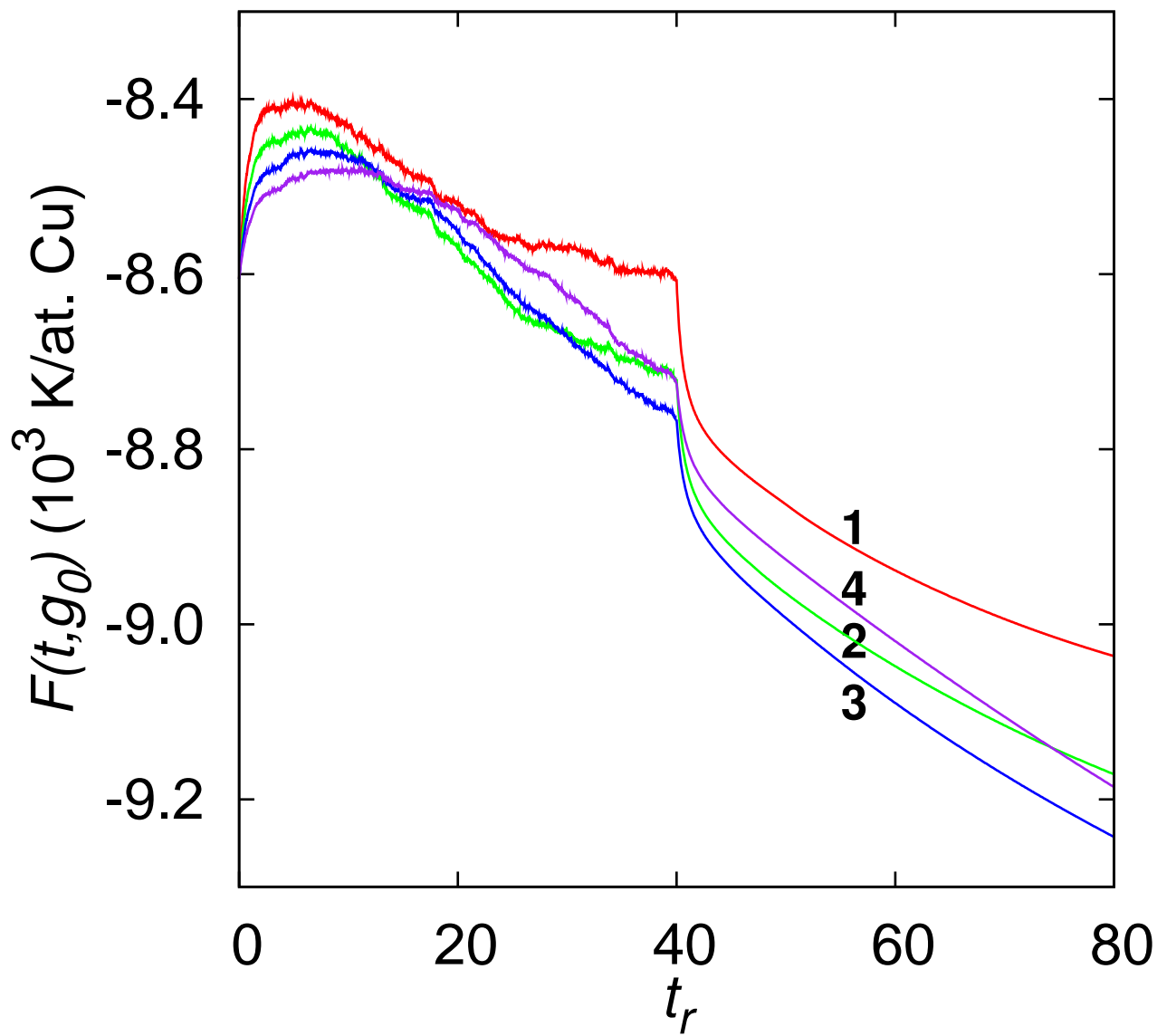
- 
- [1] L. D. Landau, E. M. Lifshits, *Statistical Physics* (Nauka, Moscow, 1995).
- [2] E.M. Lifshits, L. P. Pitaevsky, *Physical Kinetics* (Nauka, Moscow, 1979).
- [3] K. Binder, in: *Materials Science and Technology, Vol. 5: Phase Transformations in Materials*, ed. by R. W. Cahn et al. (VCH, Weinheim, 1991), Chap. 7.
- [4] F. Soisson and G. Martin, *Phys. Rev. B* **62**, 203 (2000).
- [5] M. K. Miller, B. D. Wirth and G. R. Odette, *Mater. Sci. Eng.* **353**, 133 (2003).
- [6] A. Cerezo, S. Hirose, G. Sha and G. D. W. Smith, in: *Solid→Solid Phase Transformations in Inorganic Materials 2005*, ed. by J. M. Howe et al., (TMS, Warrendale, 2005), Vol. 1, pp. 251-262.
- [7] D. Isheim, R. P. Kolli, M. E. Fine, and D. N. Seidman, *Scripta Mater.* **55**, 35 (2006).
- [8] R. Rana, W. Bleck, S.B. Singh, O.N. Mohanti, *Mater. Lett.* **61**, 2919 (2007).
- [9] Y. Wang, D. Banerjee, C. C. Su and A. G. Khachatryan, *Acta Mater.* **46**, 2983 (1998).
- [10] W. Guo, Y. Zong, G. Wang and Y. Wang, in: *Solid→Solid Phase Transformations in Inorganic Materials 2005*, ed. by J. M. Howe et al. (Ref. [6]), Vol. 2, pp. 757-762.
- [11] T. Koyama and H. Onodera, *Mater. Trans.* **46**, 1187 (2005).
- [12] T. Nagano and M. Enomoto, *Scripta Mater.* **55**, 223 (2006).
- [13] C. Zhang and M. Enomoto, *Acta Mater.* **54**, 4183 (2006).
- [14] Q. Bronchart, Y. Le Bouar, and A. Finel, *Phys. Rev. Lett.* **100**, 015702 (2008).
- [15] F. Soisson, A. Barbu and G. Martin, *Acta Mater.* **44**, 3789 (1996).
- [16] Y. Le Bouar and F. Soisson, *Phys. Rev. B* **65**, 094103 (2002).
- [17] F. Soisson and C.-C. Fu, *Phys. Rev. B* **76**, 214102 (2007).
- [18] E. Clouet, M. Nastar, A. Barbu, C. Sigli and G. Martin, *Solid→Solid Phase Transformations in Inorganic Materials 2005* (Ref. [6]), Vol. 2, pp. 683-704.
- [19] V. Yu. Dobretsov, I. R. Pankratov, A. Yu. Stroev and V. G. Vaks, *Solid→Solid Phase Transformations in Inorganic Materials 2005* (Ref. [6]), Vol. 1, pp. 169-186.
- [20] A. Yu. Stroev, I. R. Pankratov and V. G. Vaks, *Phys. Rev. B* **77**, 134203 (2008).
- [21] V. G. Vaks, *Phys. Reports* **391**, 157-242 (2004).
- [22] K.D. Belashchenko and V.G. Vaks, *J. Phys.: Condensed Matter* **10**, 1965 (1998).
- [23] V.G. Vaks, *Pis. Zh. Eksp. Teor. Fiz.* **63**, 447 (1996) [*JETP Lett.* **63**, 471 (1996)].
- [24] V. G. Vaks and K. Yu. Khromov, *Zh. Exp. Teor. Fiz.* **133**, 115 (2008) [*JETP* **106**, 94 (2008)].
- [25] V. G. Vaks and K. Yu. Khromov, *Zh. Exp. Teor. Fiz.* **133**, 313 (2008) [*JETP* **106**, 265 (2008)].
- [26] V. G. Vaks and G. D. Samolyuk, *Zh. Eksp. Teor. Fiz.* **115** 158 (1999) [*JETP* **88**, 89 (1999)].
- [27] J. W. Cahn and J. E. Hilliard, *J. Chem Phys.* **31**, 688 (1959).
- [28] V. Yu. Dobretsov and V. G. Vaks, *J. Phys.: Condensed Matter* **10**, 2261 (1998).
- [29] V. Yu. Dobretsov and V. G. Vaks, *J. Phys.: Condensed Matter* **10**, 2275 (1998).
- [30] M. Ludwig, D. Farcas, D. Pedraza, and S. Schmauder, *Modell. Simul. Mater. Sci. Eng.* **6**, 19 (1998).
- [31] F. Soisson, C. Becquart, N. Castin, C. Domain, L. Malerba, E. Vincent, *J. Nucl. Mater.*, in the press.
- [32] V. G. Vaks, S. V. Beiden, and V. Yu. Dobretsov, *Pis. Zh. Eksp. Teor. Fiz.* **61**, 65 (1995) [*JETP Lett.* **61**, 68 (1995)].
- [33] K. D. Belashchenko, I. R. Pankratov, G. D. Samolyuk and V.G. Vaks, *J. Phys.: Condensed Matter* **14**, 565 (2002).
- [34] P. Glansdorff and I. Prigogine, *Thermodynamic Theory of Structure, Stability and Fluctuations* (Wiley, 1971).
- [35] W. M. Young, and E. W. Elcock, *Proc. Phys. Soc. Lond.* **89**, 735 (1966).
- [36] T. Miyazaki, T. Kozakai and C. G. Schoen, *Solid→Solid Phase Transformations in Inorganic Materials 2005* (Ref. [6]), Vol. 2, pp. 271-290.



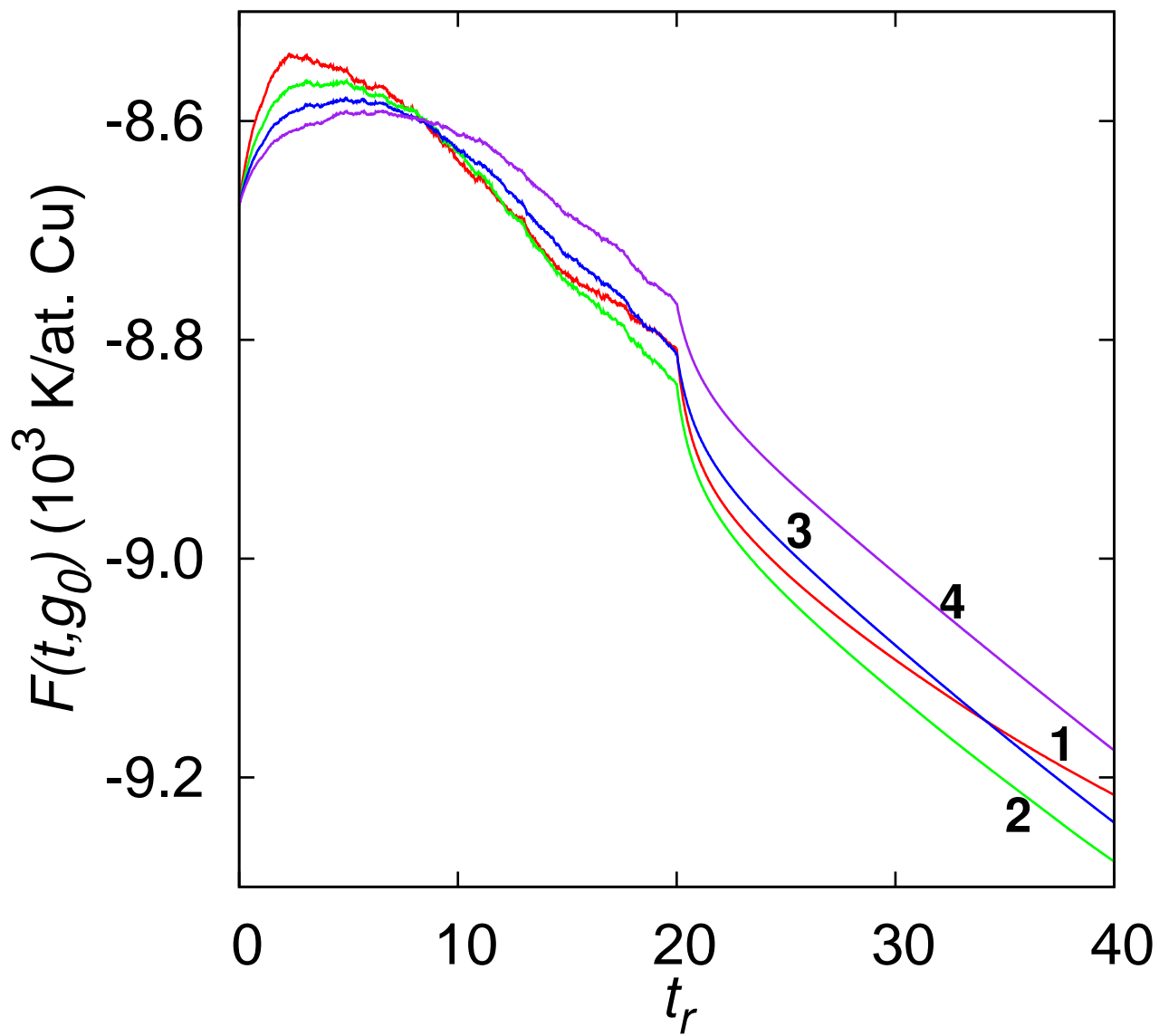


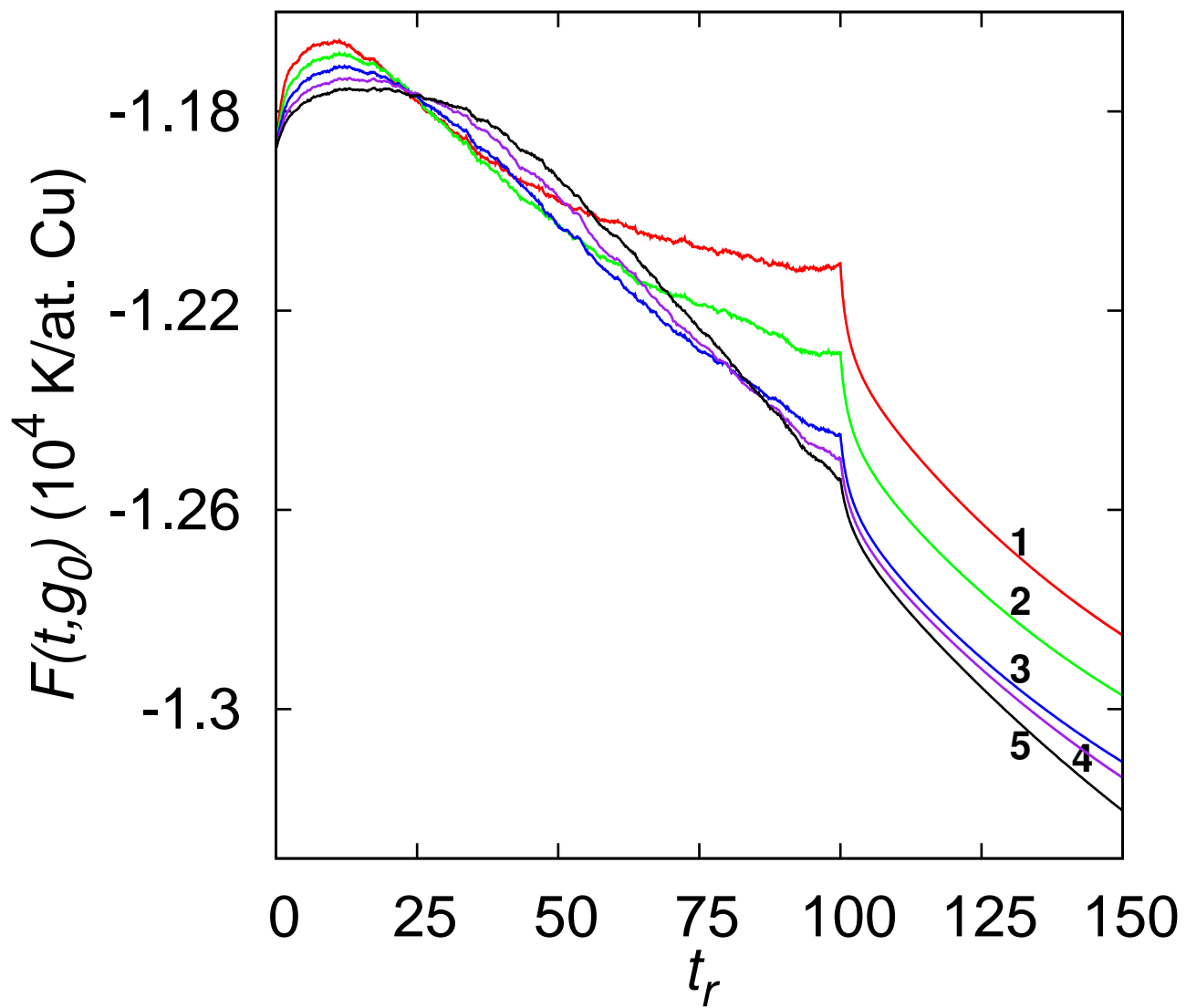


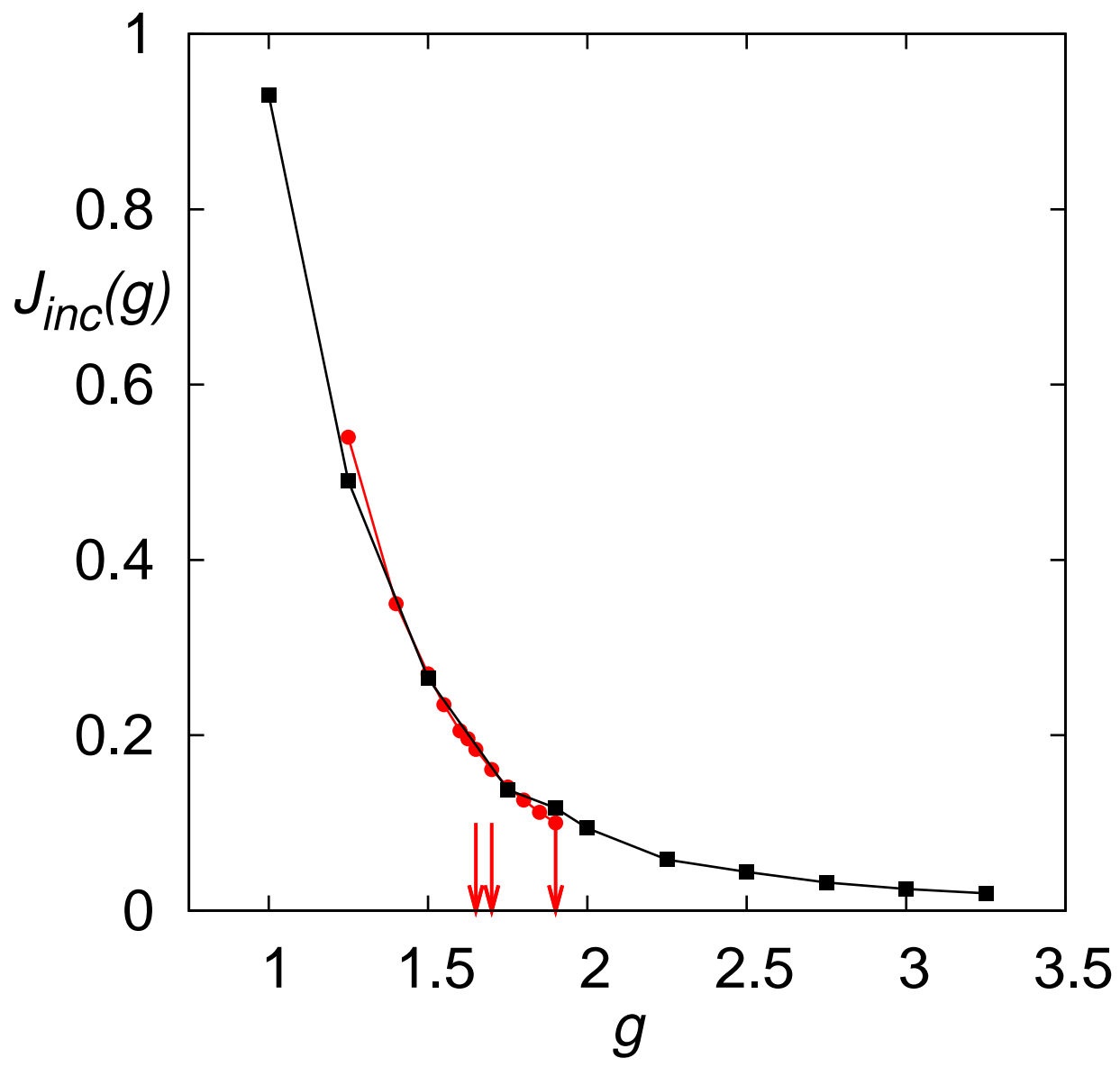


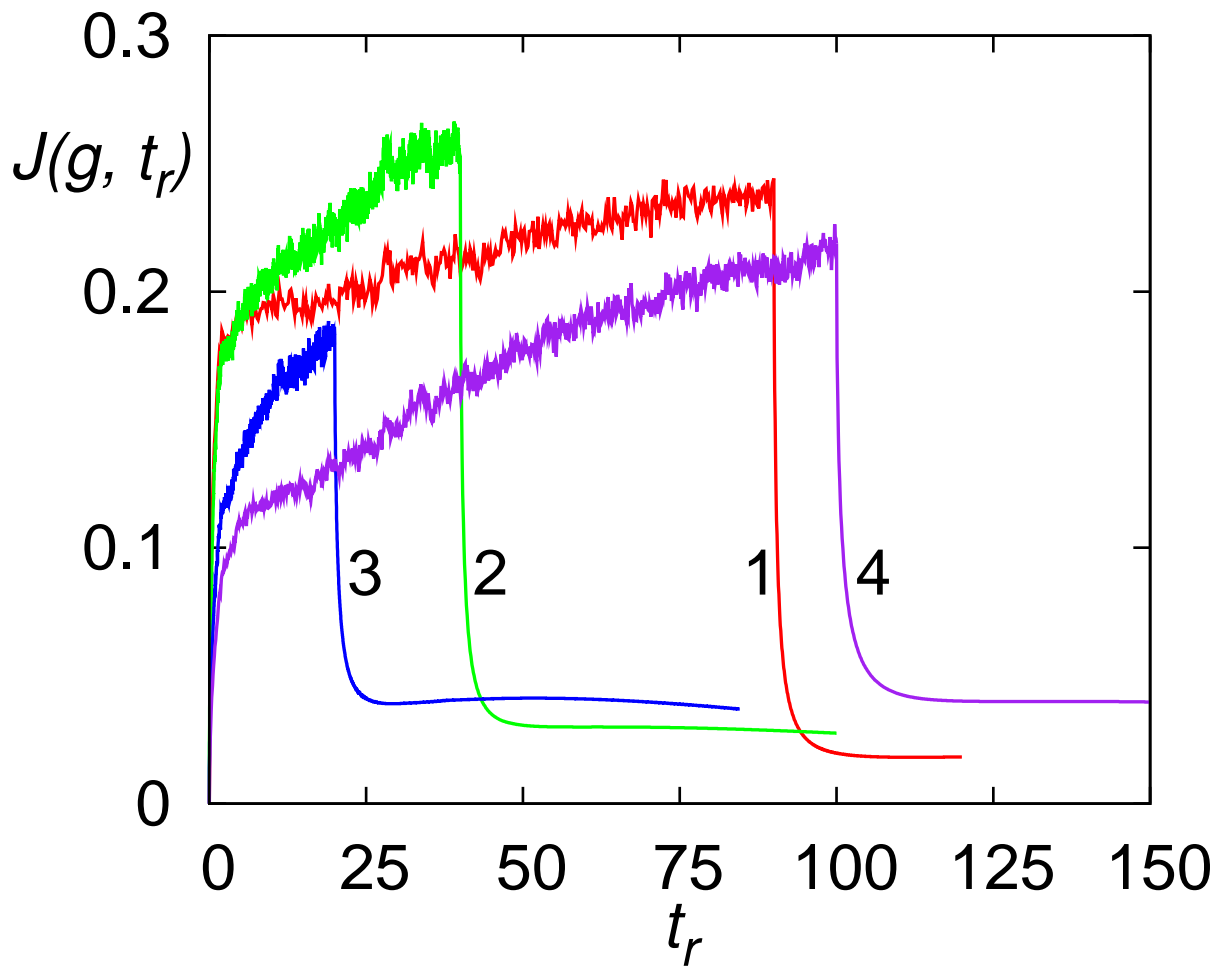


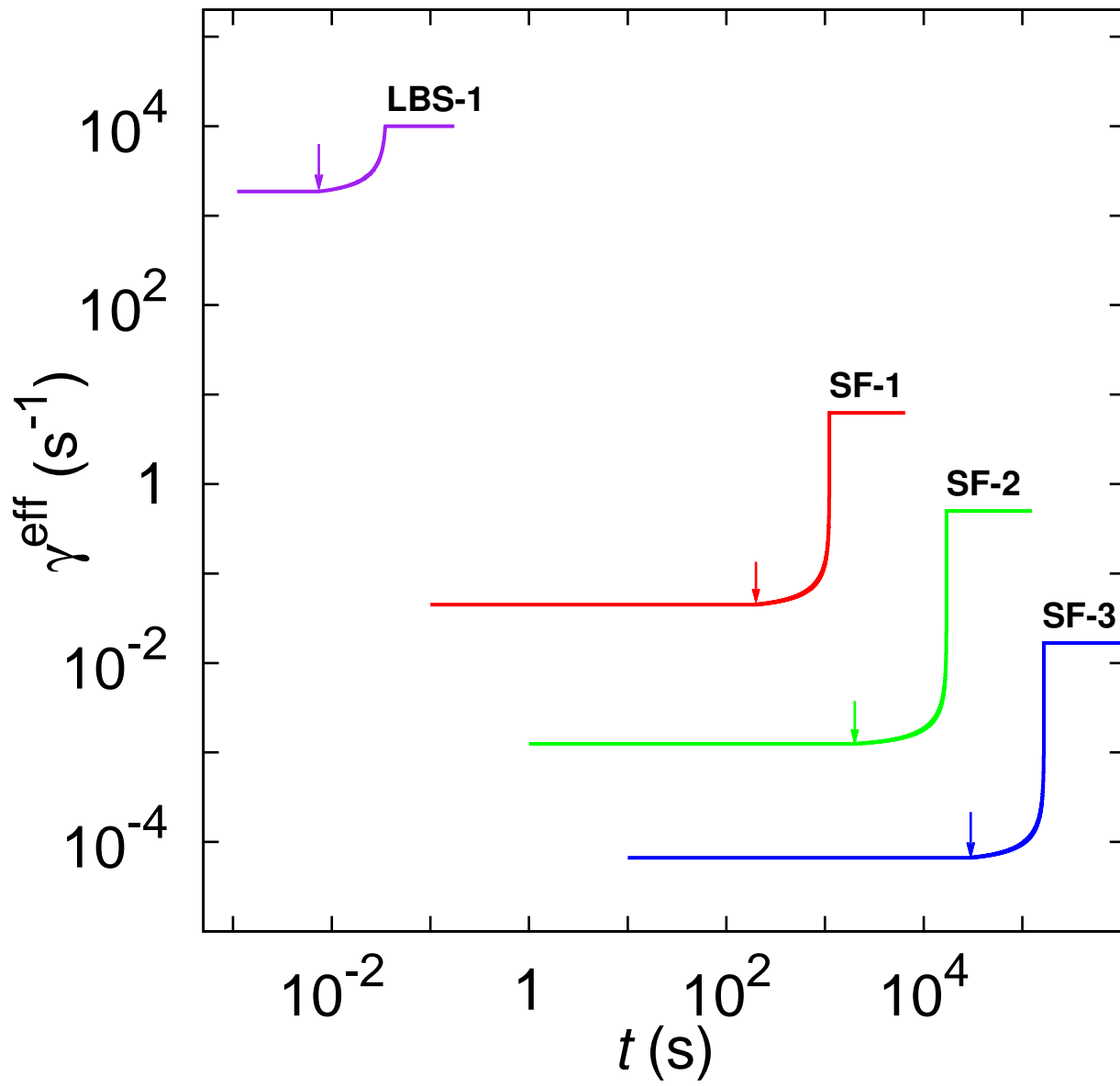


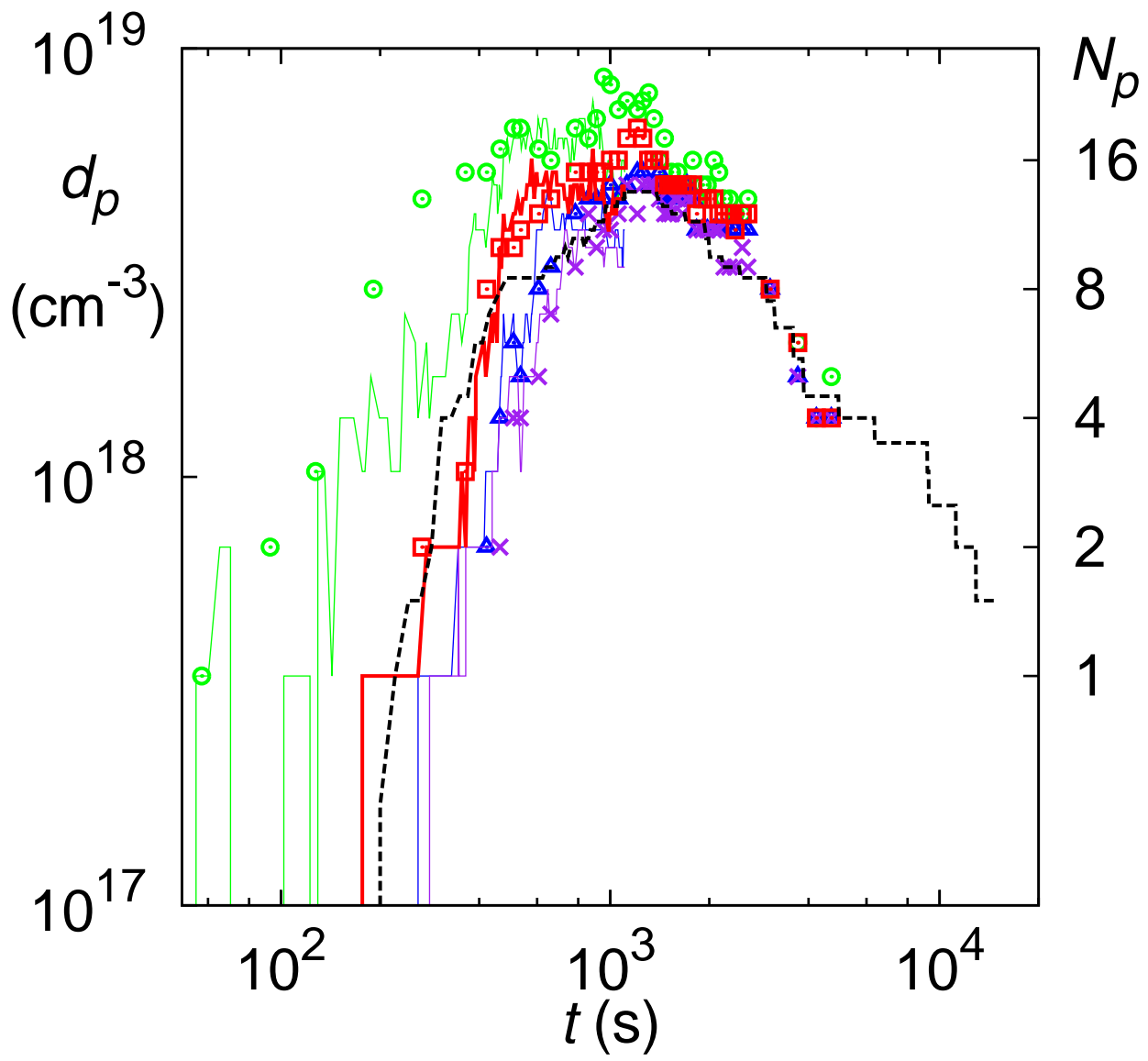


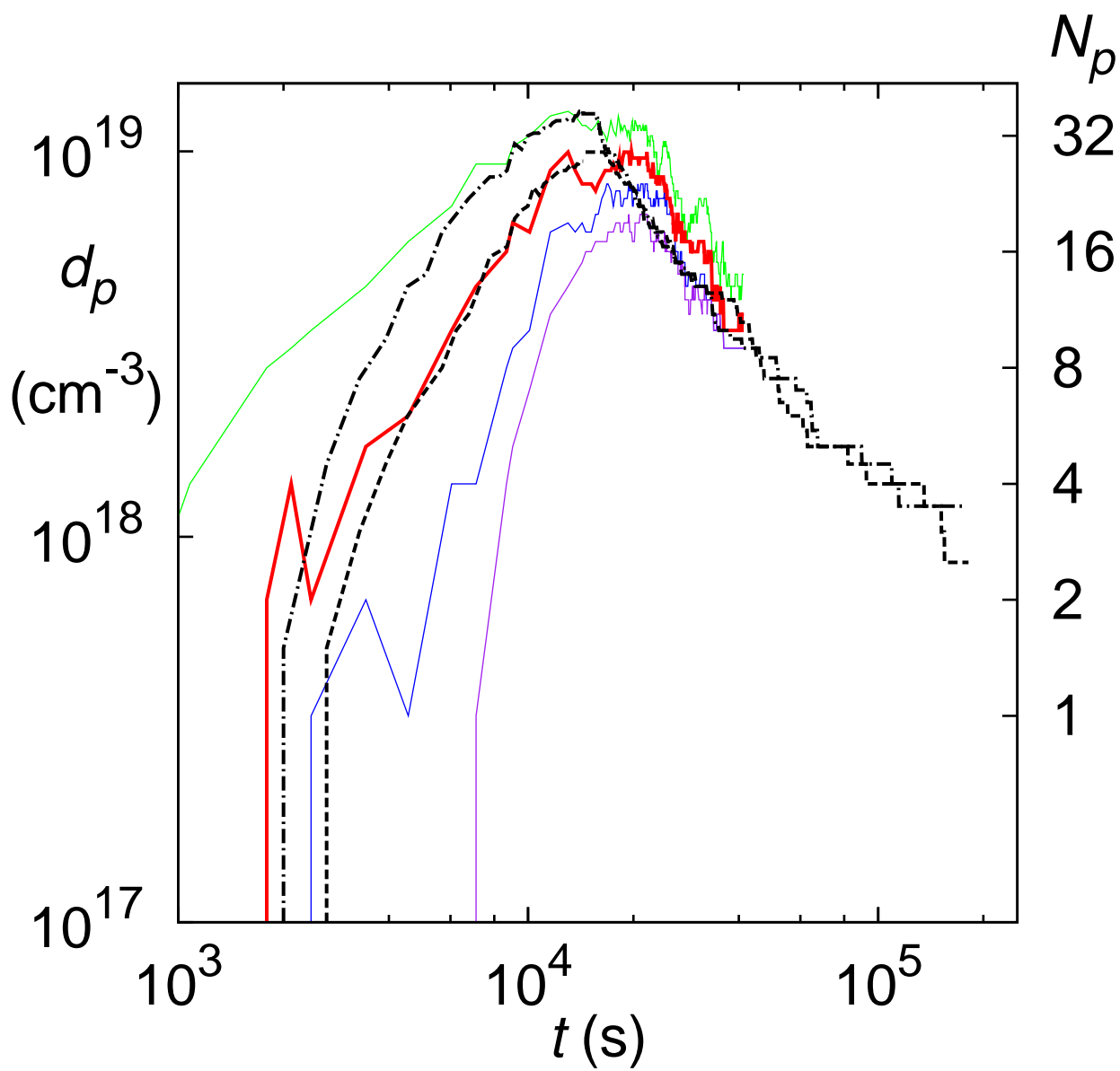


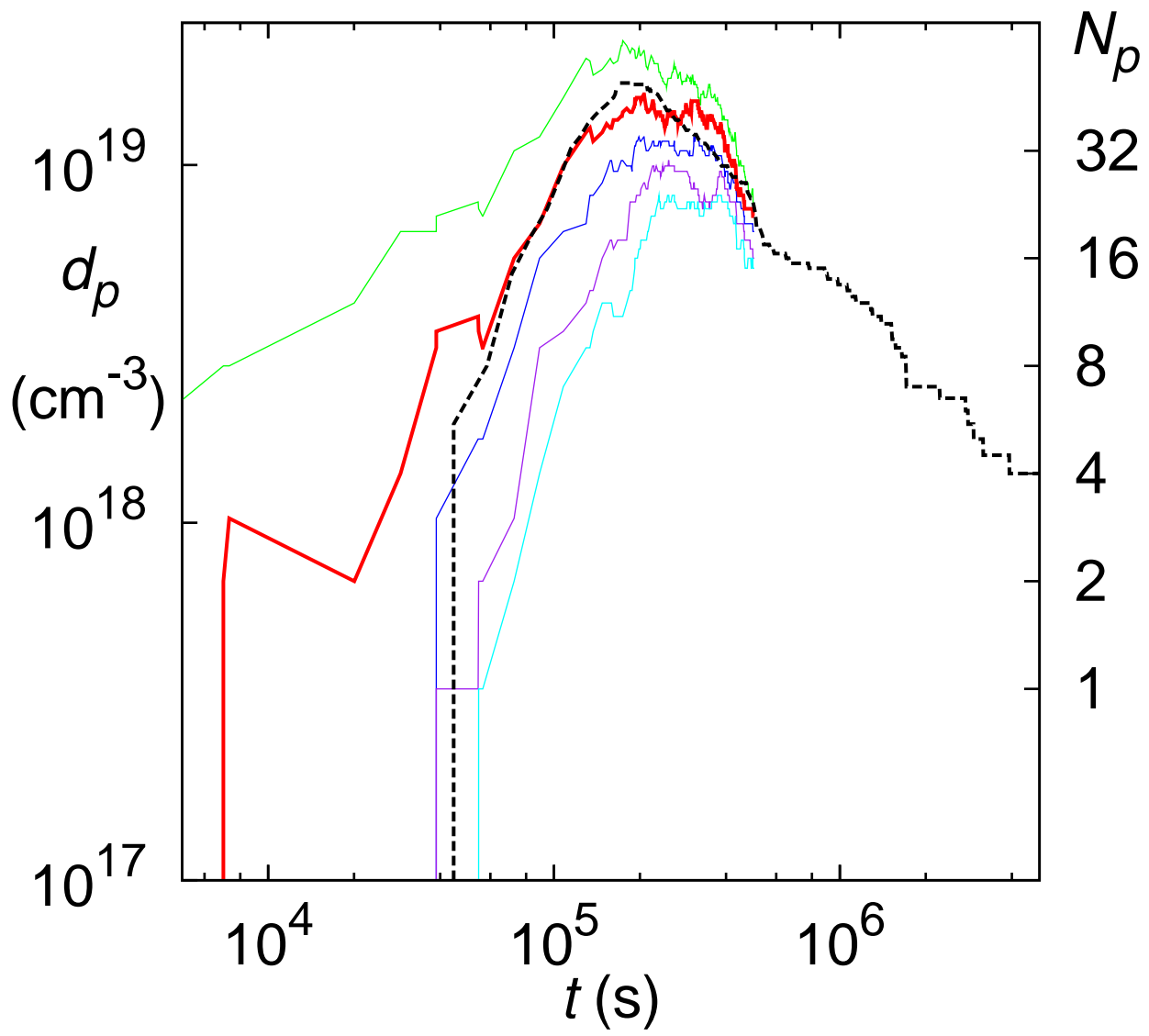




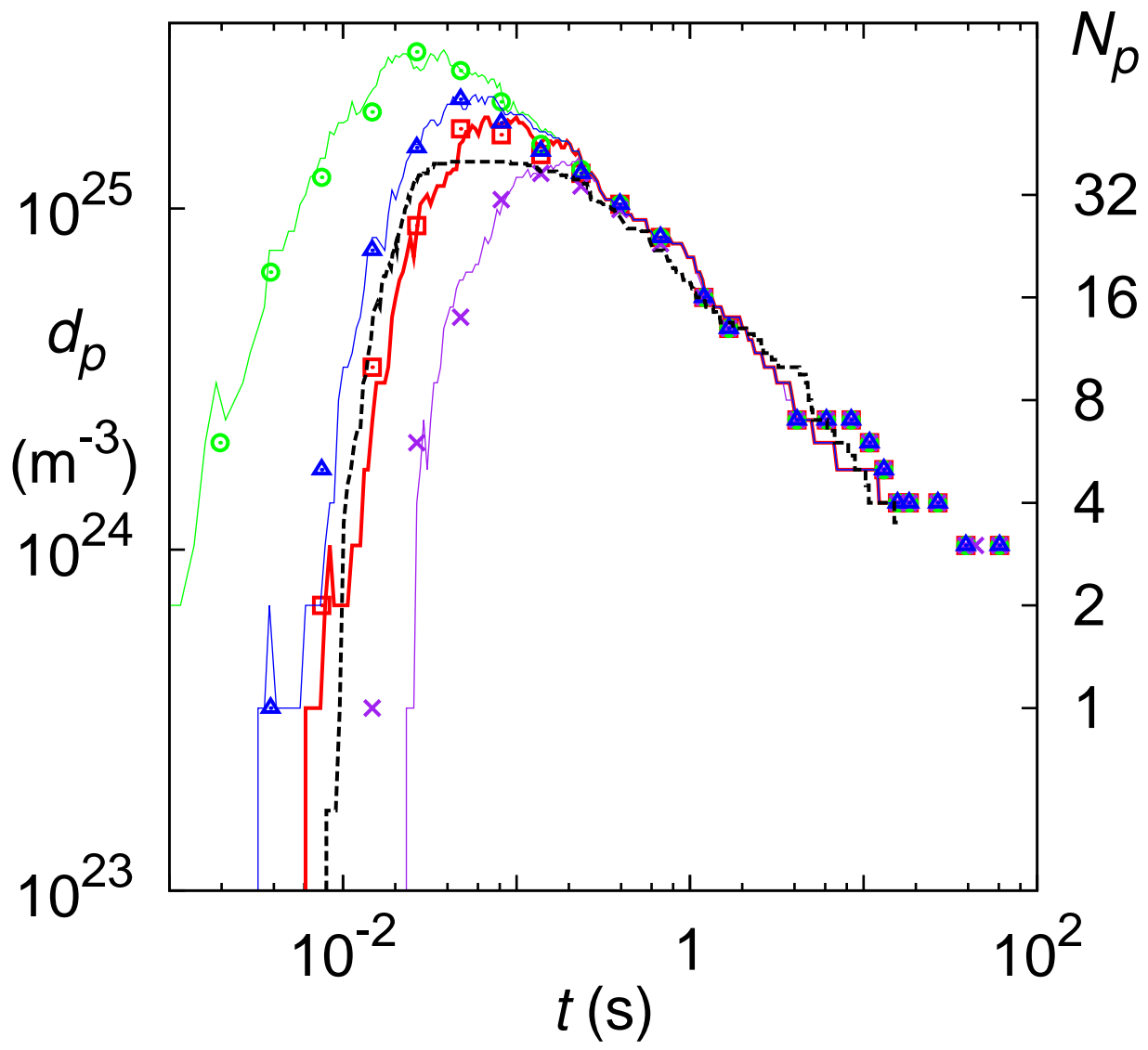


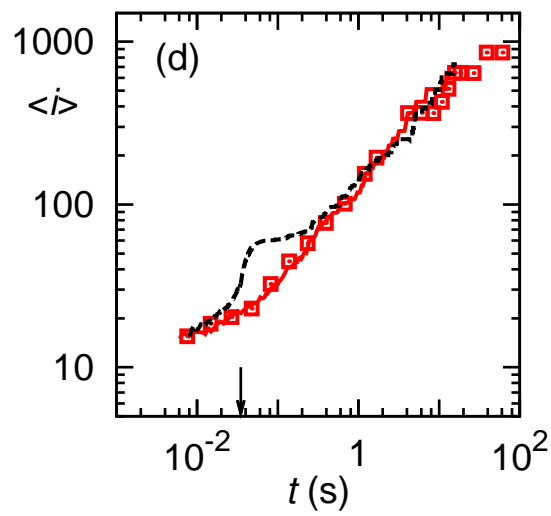
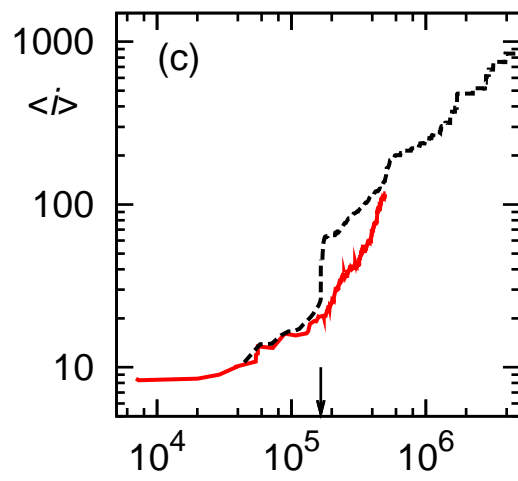
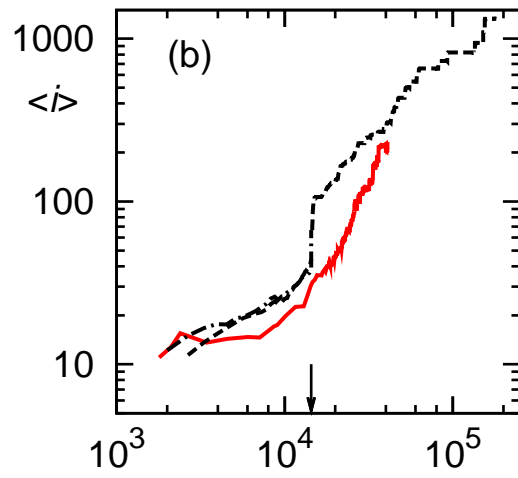
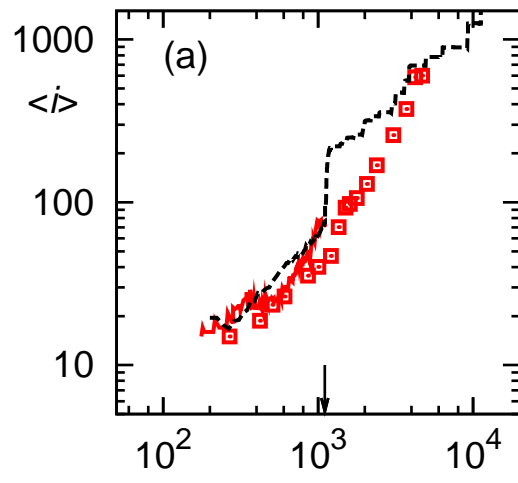












This figure "fig16.jpg" is available in "jpg" format from:

<http://arxiv.org/ps/0911.5558v2>

This figure "fig17.jpg" is available in "jpg" format from:

<http://arxiv.org/ps/0911.5558v2>

This figure "fig18.jpg" is available in "jpg" format from:

<http://arxiv.org/ps/0911.5558v2>

This figure "fig19.jpg" is available in "jpg" format from:

<http://arxiv.org/ps/0911.5558v2>

This figure "fig20.jpg" is available in "jpg" format from:

<http://arxiv.org/ps/0911.5558v2>

This figure "fig21.jpg" is available in "jpg" format from:

<http://arxiv.org/ps/0911.5558v2>



This figure "fig22.jpg" is available in "jpg" format from:

<http://arxiv.org/ps/0911.5558v2>

This figure "fig23.jpg" is available in "jpg" format from:

<http://arxiv.org/ps/0911.5558v2>